JACS
JOURNAL OF THE AMERICAN CHEMICAL SOCIETY
Article
pubs.acs.org/JACS

Redox-Dependent Structural Transformations of the [4Fe-3S] Proximal Cluster in O_2-Tolerant Membrane-Bound [NiFe]-Hydrogenase: A DFT Study

Vladimir Pelmenschikov* and Martin Kaupp*

Technische Universität Berlin, Institut für Chemie, Theoretische Chemie, Sekr. C7, Strasse des 17. Juni 135, 10623 Berlin, Germany

Supporting Information

ABSTRACT: Broken-symmetry density functional theory (BS-DFT) has been used to address the redox-dependent structural changes of the proximal [4Fe-3S] cluster, implicated in the O_2-tolerance of membrane-bound [NiFe]-hydrogenase (MBH). The recently determined structures of the [4Fe-3S] cluster together with its protein ligands were studied at the reduced $[4Fe\text{-}3S]^{3+}$, oxidized $[4Fe\text{-}3S]^{4+}$, and superoxidized $[4Fe\text{-}3S]^{5+}$ levels in context of their relative energies and protonation states. The observed proximal cluster conformational switch, concomitant with the proton transfer from the cysteine Cys20 backbone amide to the nearby glutamate Glu76 carboxylate, is found to be a single-step process requiring ~12−17 kcal/mol activation energy at the superoxidized $[4Fe\text{-}3S]^{5+}$ level. At the more reduced $[4Fe\text{-}3S]^{4+/3+}$ oxidation levels, this rearrangement has at least 5 kcal/mol higher activation barriers and prohibitively unfavorable product energies. The reverse transformation of the proximal cluster is a fast unidirectional process with ~8 kcal/mol activation energy, triggered by one-electron reduction of the superoxidized species. A previously discussed ambiguity of the Glu76 carboxylate and 'special' Fe4 iron positions in the superoxidized cluster is now rationalized as a superposition of two local minima, where Glu76-Fe4 coordination is either present or absent. The calculated 12.3−17.9 MHz ^{14}N hyperfine coupling (HFC) for the Fe4-bound Cys20 backbone nitrogen is in good agreement with the large 13.0/14.6 MHz ^{14}N couplings from the latest HYSCORE/ENDOR studies.

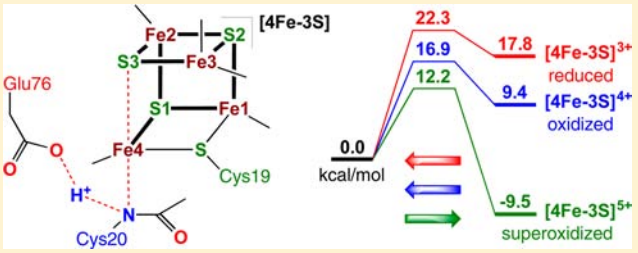

I. INTRODUCTION

Dihydrogen oxidation and evolution ($H_2 \rightleftharpoons 2H^+ + 2e^-$) in the microbial world is governed by metalloenzymes called hydrogenases.[1−5] The uptake hydrogenases provide metabolic energy by means of dividing molecular hydrogen into protons and electrons. The reverse-direction H_2-evolving enzymes consume protons and protect the cell from an excess of reductive (e^-) power during fermentation. In view of the abundant proton supply and ~440 kJ/mol H−H binding energy, nature has tightly linked H_2 chemistry with energy pathways. In contrast, industrial use of H_2 as fuel has been impeded so far by challenges in its production, storage, and efficient oxidation, thereby offering preference to fossil hydrocarbons. However, recent efforts in bioinspired catalysis, backed by improved understanding of hydrogenase function, put H_2 into focus as emerging renewable energy source.[4,6−10]

Well established in evolution already before the era of oxygenic photosynthesis, biological H_2 chemistry is commonly very sensitive to dioxygen. The most efficient natural H_2-producer known, [FeFe]−hydrogenase ($k_{cat} \sim 10^4\ s^{-1}$), is irreversibly inactivated by trace amounts of O_2.[4,11,12] Yet, several subgroups of hydrogenases are able to adapt to aerobic conditions,[13−15] such as [NiFe] enzymes hosted by Knallgas bacteria.[16] Coupled to the respiratory complex with O_2 as terminal electron acceptor, these membrane-bound hydrogenases (MBH) oxidize H_2 and generate a proton gradient between cell periplasm and cytoplasm. Remarkably, the O_2-tolerance of MBH is neither due to a modification of the active site, where the coordination of the metal pair is essentially identical to the standard O_2-inactivated [NiFe] enzymes,[17] nor due to limited access of O_2 through the hydrophobic protein gas channel.[18,19] Recent research results have indicated that a variation to one of the three iron−sulfur clusters, otherwise providing a relay for electron discharge in uptake [NiFe]-hydrogenases (Figure 1), has a pivotal role in the O_2-tolerance of MBH. This cluster, which is a canonical [4Fe-4S] cubane ~11 Å proximal to the active site in conventional [NiFe]-hydrogenases, in MBH was associated with two additional 'supernumerary' conserved cysteines.[13,20−23] Recent X-ray crystal structure determinations on the O_2-tolerant MBHs from *Ralstonia eutropha* (*Re*),[24] *Hydrogenovibrio marinus* (*Hm*),[25] and *Escherichia coli* (*Ec*)[26] bacterial species resolved an unprecedented arrangement of the proximal cluster; see Figure 2. Its inorganic [4Fe-3S] core is complemented by one of the supernumerary cysteine (Cys19) thiolates, which μ^2-bridges the Fe1 and Fe4 sites, giving a significantly distorted cubane (here and below, residue numbering from *Re* MBH is used). The second supernumerary cysteine (Cys120) completes the tetrahedral coordination of the Fe3 site.

Received: March 1, 2013
Published: July 13, 2013

 © 2013 American Chemical Society dx.doi.org/10.1021/ja402159u | *J. Am. Chem. Soc.* 2013, 135, 11809−11823

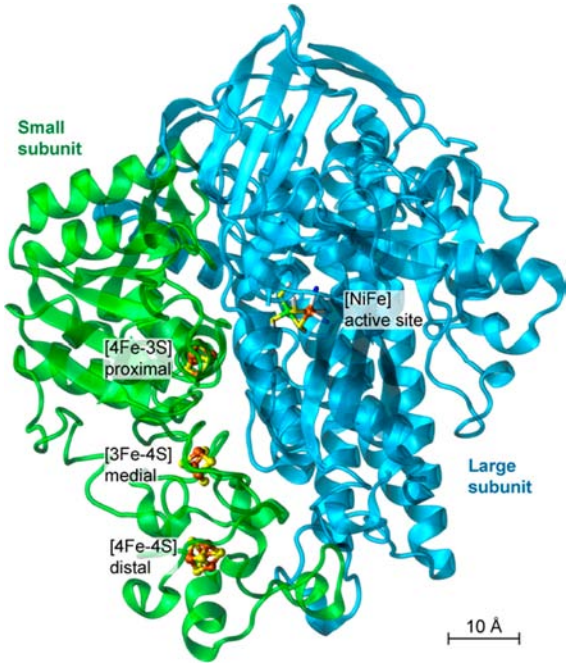

Figure 1. Overall structure of the O_2-tolerant membrane-bound hydrogenase from *Ralstonia eutropha* (PDB 3RGW). The two colored cartoons represent the structure of the heterodimer protein, and the metal cofactors are given in ball-and-stick representation. The covalent ligands in the [NiFe] active site are given as tubes.

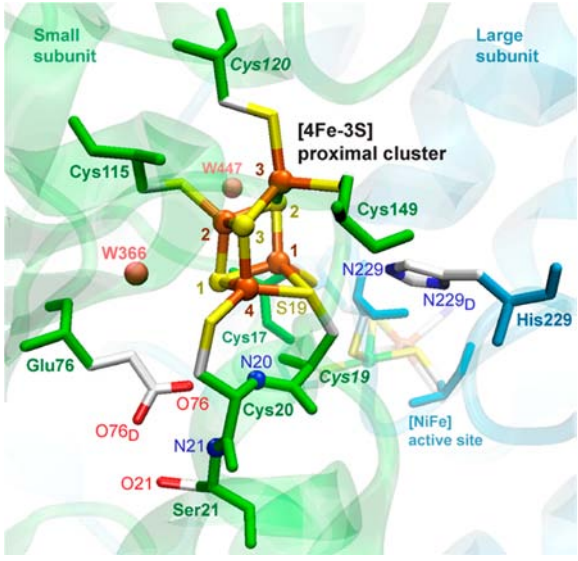

Figure 2. Detailed view of the proximal cluster from *Ralstonia eutropha* MBH under H_2-reducing conditions. The [4Fe-3S] cluster core hosted by the small subunit is given in ball-and-stick representation. The [NiFe] active site, hosted by the large subunit, is viewed in perspective. Important amino acid side chains (in color) and their backbone sections (monochrome following the subunit colors) are given as tubes. The supernumerary cysteines *Cys19* and *Cys120* are labeled in italics. The two conserved crystallographic water molecules within ~5 Å from the proximal cluster are shown as pink spheres. Individual atom labels are explained in the text, and Fe/S enumeration of the [4Fe-3S] core follows PDB 3RGW.

Recent studies on the spectroscopic species characterizing [NiFe] hydrogenases under aerobic conditions rationalize the chemistry of O_2-sensitivity vs O_2-tolerance as follows.[13,15,27,28] If O_2 attacks the reduced $[Ni^{2+}Fe^{2+}]$ species called Ni–SI, the conventional [4Fe-4S] proximal cluster of O_2-sensitive hydrogenase supplies only one electron to the active site. This results in the 'unready' Ni-A state, which is a pitfall for the enzyme activity.[29−33] The bridging hydroperoxo $[Ni^{3+}\text{-}^{-}OOH\text{-}Fe^{2+}]$ species proposed as Ni-A candidate[5,29,34,35] is then in line with the electron count. In contrast, the Fe–S clusters relay in O_2-tolerant MBH (Figure 1) is capable of providing three electrons to the [NiFe] site, producing the rapidly (~1 s) self-activating 'ready' $[Ni^{3+}\text{-}^{-}OH\text{-}Fe^{2+}]$ species[5,31,32,34,36,37] called Ni–B (and one H_2O molecule as byproduct).[20,38] During the Ni–B formation by MBH, two electrons are provided by the modified proximal [4Fe-3S] cluster,[39] and one electron comes from the medial [3Fe-4S] cluster.

Taken together, the available results suggest that the proximal [4Fe-3S] cluster carries out a dual task in MBH: while this unique cofactor conducts electrons away from the [NiFe] center during H_2 oxidation, it also supplies *two electrons* in the reverse direction upon binding of O_2 at the active site, thus avoiding the harmful Ni-A species. The cluster is thus capable of cycling between three oxidation levels, reduced S = 1/2 $[4Fe\text{-}3S]^{3+}$, oxidized S = 0 $[4Fe\text{-}3S]^{4+}$, and superoxidized S = 1/2 $[4Fe\text{-}3S]^{5+}$.[21,39] The extraordinary conformation of the reduced cluster called 'RED' in Figure 3 is, however, not sufficient by itself to promote the two-electron $[4Fe\text{-}3S]^{3+} \rightleftharpoons [4Fe\text{-}3S]^{5+}$ transition within the physiologically relevant, narrow (~0.2 V) range of redox potentials.[27,39−41] In the 'high-potential' $[1Fe^{2+}3Fe^{3+}]$ superoxidized state, backbone amide N20 from the Cys19-Cys20 'short spacer unit' becomes deprotonated and coordinates to Fe4, resulting in a loss of the Fe4–S3 bond and enhanced cluster opening, shown as conformation 'S-OX' in Figure 3.[25,26] Deprotonation of the amide N20 has been implicated in stabilization of the highly positive $[4Fe\text{-}3S]^{5+}$ core, and in proton-coupled electron transfer (PCET).[25,26,42] Tentative long-range proton-transfer pathways originating at N20 were debated, leading either to the [NiFe] active site to form the Ni–B species or to the protein surface, with a consensus on the Glu76 carboxylate as an initial proton acceptor.[25,26]

A recent study[26] further indicated a redox-dependent mobility of the Glu76 side chain. In the RED structure, one of the carboxylate oxygen atoms O76 is ~4.7 Å from the 'special' Fe4 site; see Figure 2. For the superoxidized cluster, refinement of the X-ray data collected on the MBHs from *Ec*[26] and *Hm*[25] exposed two alternative positions for both Glu76 and Fe4, with Fe4–O76 distances of ~4.1 Å and ~2.1 Å, corresponding to a splitting of the S-OX conformation into $S\text{-}OX_D$ and $S\text{-}OX_P$, respectively (Figure 3; here and below, we append D/P subscripts implying the Glu76 carboxylate, respectively, distal or proximal to Fe4). In $S\text{-}OX_D$, the glutamate side chain occupies a position similar to the one in RED_D.

As remarked earlier, coordination of the Cys20 amide and Glu76 carboxylate to the $[4Fe\text{-}3S]^{5+}$ core in the $S\text{-}OX_P$ state allows parallels to be drawn between the MBH proximal cluster and the P-cluster of nitrogenase.[14,24,25,42] The [8Fe-7S] P-cluster can be viewed as two [4Fe-3S] subclusters, bridged by the central inorganic sulfide and two cysteine μ^2-thiolates. In analogy to the [4Fe-3S] cluster of MBH, one of the P-cluster subunits reversibly attracts protein nitrogen (from a Cys backbone) and oxygen (from a Ser side chain) ligands upon two-electron ($P^N \rightarrow P^{OX}$) oxidation, at the same time resulting in (partial) loss of two Fe–S bonds.[43]

dx.doi.org/10.1021/ja402159u | J. Am. Chem. Soc. 2013, 135, 11809−11823

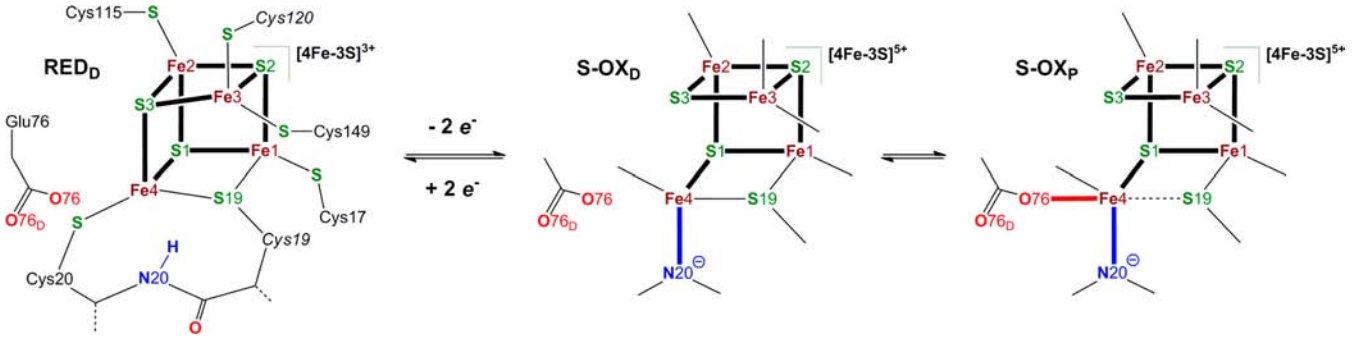

Figure 3. Schematic comparison of the MBH proximal cluster in structurally characterized reduced RED$_D$ (PDB 3RGW, 3AYX, 3UQY) vs two-electron superoxidized S-OX$_D$ and S-OX$_P$ (PDB 3AYY, 3USC) states. The Fe−S bonds of the [4Fe-3S] core are given in black bold. The colored bonds indicate Glu76 carboxylate O76 oxygen (red) and Cys20 backbone N20 nitrogen (blue) coordination to the Fe4 iron site in the S-OX states. The supernumerary cysteines *Cys19* and *Cys120* are labeled in italics. The dashed Fe4−S19 bond in S-OX$_P$ indicates a contact at ∼2.9 Å. The amino acid and inorganic Fe/S atom numbering corresponds to PDB 3RGW.

Only a few computational studies on the novel proximal cluster have been reported so far,[26,44,45] all using broken-symmetry density functional theory (BS-DFT). Mostly focused on a comparison of the calculated ^{57}Fe−Mössbauer parameters to the experimental values on MBH from *Aquifex aeolicus* (*Ae*),[39,45] these studies rationalized the electronic structure of the [4Fe-3S] core. While consensus was established on the ferric (Fe^{3+}) character of the 'special' Fe4 site for the superoxidized cluster, the spin-coupling schemes between the four Fe sites remained debated.[46,47] The first QM/MM modeling[26] of the S-OX$_{D/P}$ structures proposed that the Glu76 orientation ambiguity results from a difference in protonation state. While the deprotonated Glu76 carboxylate was used for S-OX$_D$ (this model has been named PC3$_d^-$), the carboxylate O76$_D$ oxygen atom distal to Fe4 was suggested to be protonated in S-OX$_P$, resulting in a penta-coordinated Fe4 site (model PC3^H) with the optimized Fe4−S19 distance of 2.46 Å. However, the expansion of the Fe4−S19 distance to ∼2.9 Å, as refined for the S-OX$_P$ X-ray structure, indicates only a weak noncovalent Fe−S interaction, and thus an essentially tetrahedral Fe4 coordination. The long Fe4−S19 distance in S-OX$_P$ was better reproduced by QM/MM only when using the deprotonated Glu76 carboxylate (model PC3$^-$). Another DFT study[45] indicated that the protonated Glu76 carboxylate is structurally unreasonable for their models of the reduced and superoxidized cluster, and argued the role of Glu76 as proton acceptor from the N20 amide. Interestingly, in a follow-up QM/MM study[44] it was concluded that the proton transfer from the N20 amide to the Glu76 carboxylate is favorable at the [4Fe-3S]$^{4+}$ oxidation level, when using a reactant structure with 'opened' S-OX cluster core (model PC2[N−H,E76$^-$]). This computational result therefore raises a relevant concern regarding structural stability of the proximal cluster during its 'normal' [4Fe-3S]$^{3+}$ ⇌ [4Fe-3S]$^{4+}$ redox transition, linked to the H_2 catalysis.

The plasticity of the [4Fe-3S] proximal cluster core within the framework of six cysteines, together with the mobility of the Glu76 side chain, creates a puzzling structural manifold. As interpretation of the X-ray diffraction data is nontrivial for multicenter metal cofactors in proteins, and protonation states can commonly be deduced only indirectly, we use the power of DFT analysis to study the two-way RED ⇌ S-OX redox-dependent transformation of the proximal cluster at its detailed atomistic level. Understanding the spin-dependent electronic structure of the cluster allows us to reproduce the hyperfine coupling parameters, now available for the Fe4-bound N20 backbone amide from ENDOR and HYSCORE studies.[27,48] Finally, we examine the performance of DFT methods for this unique iron−sulfur center.

II. COMPUTATIONAL METHODS

A. Density Functional Methods. The calculations were done using the PBE[49,50] and B3LYP[51,52] functionals as indicated in the text, and the LACV3P** basis set as implemented in the JAGUAR 7.8 software.[53] For the first- and second-row elements, LACV3P** implies 6-311G** triple-ζ basis sets including polarization functions. For the Fe atom, LACV3P** consists of a triple-ζ quality basis set for the outermost core and valence orbitals, and the quasirelativistic Los Alamos effective core potential (ECP) for the innermost 10 electrons.[54] Broken-symmetry (BS, see also below)[55,56] initial guesses were obtained in JAGUAR 7.8. The guess orbitals were then exported to GAUSSIAN 09[57] for structure optimizations of local minima and transition states. During the optimization, certain polypeptide α-carbon (C_α) atoms were fixed to their positions from the X-ray diffraction structure, as described further below. This approach has been shown to perform well for minima and transition states when modeling protein cofactors, including iron−sulfur clusters,[58−60] even though the stationary points are of course approximate. Firmer grounds for C_α fixations around the proximal cluster are given in the next section. Unless stated otherwise, the protein environment of the proximal cluster was considered via self-consistent reaction field (SCRF) polarizable continuum model using the integral equation formalism (IEF-PCM)[61] as implemented in GAUSSIAN 09, with the static dielectric constant set to ε = 4.0, as often used for proteins, and the remaining IEF-PCM parameters at their default values for water. The SCRF molecular cavity was built using UFF atomic radii scaled by 1.1. Unless stated otherwise, no dispersion corrections were used. However, to estimate how important dispersion interactions may be for structure and energetics, a number of calculations used the two-body D3 dispersion corrections by Grimme et al.[62,63] as implemented in JAGUAR 7.8, as pointed out in the Results section.

B. Broken-Symmetry States. Depending on the oxidation level of the proximal cluster, the formal number of ferrous (Fe^{2+}, d^6, S = 2) and ferric (Fe^{3+}, d^5, S = 5/2) iron sites in the [4Fe-3S] core varies: [3Fe^{2+}1Fe^{3+}] for the S = 1/2 reduced state, [2Fe^{2+}2Fe^{3+}] for the S = 0 oxidized state, and

dx.doi.org/10.1021/ja402159u | J. Am. Chem. Soc. 2013, 135, 11809−11823

$[1Fe^{2+}3Fe^{3+}]$ for the $S = 1/2$ superoxidized state. Following the well-known BS-DFT approach[55,56] to multicenter transition-metal clusters, parallel (ferromagnetic) or antiparallel (antiferromagnetic) alignments of the Fe*i* iron site spins S_i, $i = 1...4$, were considered here within an unrestricted Kohn−Sham framework, satisfying the relation $\sum M_{Si} = M_S$ for the spin-projection numbers. Using $M_{Si} = \pm S_i$ corresponding to the high-spin Fe sites and $M_S = S$ for the total spin projection of the cluster with S_i and S as detailed above, we obtain a [2Fe↑:2Fe↓] BS pattern which applies to all three oxidation levels, where '↑' and '↓' denote $M_{Si} > 0$ and $M_{Si} < 0$, respectively. These considerations result in $4\cdot(4-1)/2 = 6$ possible selections of the [2Fe↑]/[2Fe↓] pairs among the four Fe ions. In the following, we denote these configurations by BS*ab*, according to the [2Fe↓] site numbers carrying excess local spin antiparallel to the total spin of the cluster, that is, $M_{Sa} < 0$ and $M_{Sb} < 0$. The predefined signs of M_{Si} usually remain stable during self-consistent field (SCF) convergence and structure optimization. The identity of the Fe^{3+}/Fe^{2+} oxidation states within the [2Fe↑] and [2Fe↓] pairs is, however, often lost during the calculation due to a characteristic spin delocalization in iron−sulfur clusters.[64,65] This leads to mixed-valence pairs where the formal oxidation state of each iron site is $Fe^{2.5+}$ on average. Therefore, BS*ab* = BS*ba*, and the configurations available read as BS12, BS13, BS14, BS23, BS24, and BS34. This BS classification is equivalent to the one applied earlier by Volbeda et al.[26] For the diamagnetic $S = 0$ $[2Fe^{2+}2Fe^{3+}]$ oxidation level, these six configurations effectively reduce to three: BS12, BS13, and BS14. The spin density distributions in these three BS states are exactly opposite to those of BS34, BS24, and BS23, respectively. For the proximal cluster models at the three $[4Fe\text{-}3S]^{3+/4+/5+}$ oxidation levels, the above BS states were computationally constructed in JAGUAR 7.8 using an option to assign the number of unpaired α/β electrons to Fe atomic fragments, and their structures were then optimized using GAUSSIAN 09. As described below, we will report mainly BS12 results, unless otherwise stated. However, as three recent BS-DFT studies favored either the BS13 or BS34 states,[26,44,45] based on comparison with ^{57}Fe−Mössbauer parameters, we also examine how choosing either of these two states will modify our results, in particular regarding the energetics of the mechanism for structural transformation.

C. Spin Coupling and Hyperfine Interaction. As described elsewhere,[66−69] a spin-vector coupling model operating in terms of the main S_i and S spin numbers (in contrast to M_S for the BS states) is necessary to reproduce the hyperfine coupling (HFC) interaction parameters available[27,48] for the ^{14}N nuclei of the $[1Fe^{2+}3Fe^{3+}]$ $S = 1/2$ superoxidized cluster. Based on the spin-projection scheme proposed below in Results, the raw BS-DFT HFC tensors calculated for the Fe4-bound N20 nitrogen atom are then scaled by the projection coefficient $P_{N20} = 7/15 \approx 0.47$, as described in Supporting Information. This results in the calculated $A^{DFT}(^{14}N)$ tensors discussed below.

III. RESULTS

We start with the detailed analysis of the protein environment around the proximal cluster and our DFT modeling setup. This is followed by rationalization of the available X-ray structures, and then by the detailed consideration of the RED ⇌ S-OX cluster rearrangement mechanism. Further, reorganization energies of the proximal cluster are estimated and significance of the dispersion interaction is evaluated. The electronic structure of the [4Fe-3S] core is then considered with an emphasis on the BS states. Finally, based on the spin-coupling analysis, we discuss the hyperfine coupling tensor $A^{DFT}(^{14}N20)$ for the N20 nitrogen atom coordinated to the 'special' Fe4 iron of the $S = 1/2$ superoxidized cluster.

A. Proximal Cluster Environment. Both first shell amino acid ligands to the [4Fe3S] core and second shell hydrogen bonding partners from the protein are important in accurate DFT modeling of the proximal cluster. The cluster environment introduced above and further detailed below for *Re* MBH is mostly conserved for the known members of this hydrogenase family. The amino acids involved in coordination of the four Fe ions are the six cysteines (Cys 17, 19, 20, 115, 120, 149) and Glu76 from the small protein subunit. His229 imidazole provides the closest contact to the proximal cluster from the neighboring large subunit (S17/S19/Fe1−N229 ∼3.3/3.7/4.2 Å, see Figure 2). Additionally, two conserved crystallographic water molecules W366 and W447 are within ∼5 Å from the [4Fe-3S] core, weakly coordinated at the [Fe2−Fe4−S1−S3] and [Fe1−Fe2−S1−S2] faces of the distorted cubane. The highly polar water (bulk $\varepsilon = 80$) molecules are expected to effectively reduce the energy cost of the $[4Fe\text{-}3S]^{3+/4+/5+}$ redox transitions. The Glu76 carboxylate, implied in deprotonation of the N20 backbone nitrogen atom,[25,26] participates in a complex hydrogen-bonding network involving Trp11, His13, Cys20, and Ser21. Among these residues, Ser21 (Thr21 in the MBH from *Ec*) provides the key contacts to the Glu76 carboxylate oxygen atoms in the H_2-reduced structure (O76−N21 ∼2.8 Å and $O76_D$-O21 ∼2.5 Å, see Figure 2).

B. Reduced State and Modeling Aspects. The H_2-reduced state RED_D in Figures 2 and 3 was characterized by independent X-ray experiments on MBHs from three organisms, namely, *Re*,[24] *Hm*,[25] and *Ec*.[26] RED_D therefore provides the structural reference for the proximal cluster modeling. Following the considerations above in **A**, our DFT model includes the nine important amino acid side chains shown in Figure 2, the Cys19-Cys20-Ser21 backbone spacer, and the two X-ray water molecules W366 and W447. With the exception of the α-carbon atom of Cys20 within the backbone spacer, the 'broken' polypeptide links of the eight remaining terminal C_α carbon atoms were saturated by hydrogen atoms and fixed to their crystallographic positions during structure optimization. To provide a firmer ground to the fixing of the C_α atoms, we assessed the flexibility of the polypeptide framework around the proximal cluster during the redox-dependent rearrangement of the [4Fe-3S] core. Using the available *Re* and *Hm* MBH X-ray structures, Table S1 in Supporting Information maps the $9\cdot(9-1)/2 = 36$ C_α-C_α distances present in our model. For the *Re* vs *Hm* RED structures, C_α-C_α distances vary commonly by less than 0.1 Å between the two analyzed MBH species. The analysis of the RED vs S-OX structures from the *Hm* species indicates that the selected α-carbon atoms shift commonly by less than 0.2 Å relative to each other upon the RED ⇌ S-OX transition; the most significant 0.3 Å C_α-C_α change during the redox process was found for the two C_α^{Cys20}-C_α^{Glu76} and C_α^{Cys20}-C_α^{Cys115} distances involving the Cys20 α-carbon atom (which was not fixed during optimization).

The modeling setup described above leaves alternatives for the protonation states of the Glu76 carboxylate ε-oxygen atoms and the His229 imidazole δ- and ε-nitrogen atoms. Negative carboxylate and neutral imidazole side chains are natural assumptions corresponding to the neutral pH = 7 level. In the

RED_D structure, the O76 carboxylate oxygen atom is hydrogen-bonded to N21 from the backbone and therefore cannot carry a proton. The second carboxylate oxygen atom $O76_D$ is hydrogen-bonded to the O21−H hydroxy group of the Ser21 γ-oxygen site (Thr21 γ-oxygen in the *Ec* MBH) and was set to be deprotonated as well. The $N229_D$ δ-nitrogen atom distal to the proximal cluster does not have apparent hydrogen bonding partners within the His229 imidazole ring plane and was left deprotonated. Therefore, the ε-nitrogen atom, which provides a weak S17−N229 ∼3.3 Å hydrogen-bonding contact to the sulfur atom of Cys17, was protonated. Our RED_D^{3+} DFT model carries a total 4-fold negative charge and contains 102 atoms. To reflect the cluster oxidation level, we append 3+/4+/5+ superscript indexes to our model names, corresponding to the $[4Fe\text{-}3S]^{3+/4+/5+}$ core charge, respectively.

The RED_D^{3+} model optimized using the PBE functional is overlaid with its initial structural reference from PDB 3RGW[24] in Figure 4a, showing that the present protonation scheme and DFT methodology together permit a realistic description of the proximal cluster. Selected internuclear (including nonbonding) distances from the modeling and X-ray structures are compared in Table 1. They exhibit deviations of ∼0.1 Å at most. However, the two loosely bound crystallographic water molecules W366 and W447 shift their positions by ∼0.5 and ∼2.6 Å, respectively. Importantly, attempts to modify (*i*) the above protonation scheme for Glu76 and His229 and (*ii*) the DFT methodology provided somewhat worse agreement with the experimental RED_D structures. For (*i*), this is reflected in increased displacements of the Glu76, His229, and Ser21 side chains. In case (*ii*), we notice that omission of the SCRF solvent leads to an expansion of the cluster model due to the large negative charge. Using the popular B3LYP hybrid functional rather than the pure generalized gradient approximation (GGA) PBE functional led to a noticeable overestimation of the Fe−Fe/Fe−S distances, as detailed in Figure S1 and Table S2 of Supporting Information. Similar observations on the performance of B3LYP vs some pure GGA functionals (such as PBE, PW91, or BP86) for metal−ligand structural data were noticed earlier,[70−72] including that of metalloenzyme active sites.

C. Superoxidized State. In contrast to the RED_D structure which was characterized after the protein reduction by H_2, the S-OX structures for two enzymes from *Hm* and *Ec*, determined upon air or chemical oxidation, display an ambiguous conformation of the proximal cluster.[24−26] As discussed above, the two $S\text{-}OX_{D/P}$ alternatives shown in Figure 3 arise from the refinement.[26] In order to obtain the S-OX states computationally, two electrons were removed from the optimized RED_D^{3+} model described in **B** above.

All our models were thus based on the same 3RGW PDB structure, and the necessary modifications prior to optimization of the $S\text{-}OX_{D/P}$ candidates are detailed below.

S-OX$_D^{5+}$. The key structural change during the transition from RED_D to $S\text{-}OX_D$ is coordination of the N20 backbone amide to Fe4 (Figure 3). To describe the $S\text{-}OX_D^{5+}$ state, N20 was therefore first deprotonated. This resulted in spontaneous ∼1.4 Å contraction of the Fe4−N20 distance during the optimization to ∼2.0 Å. Concomitantly, the ∼2.4 Å Fe4−S3 coordination present in the RED_D^{3+} state was lost, with a final Fe4−S3 distance of ∼4.3 Å. The optimized $S\text{-}OX_D^{5+}$ model correlates well with the X-ray structural data for the $S\text{-}OX_D$ proximal cluster from *Hm* and *Ec* MBHs[25,26] (Figure 4b). The agreement with any of these two structures is, however,

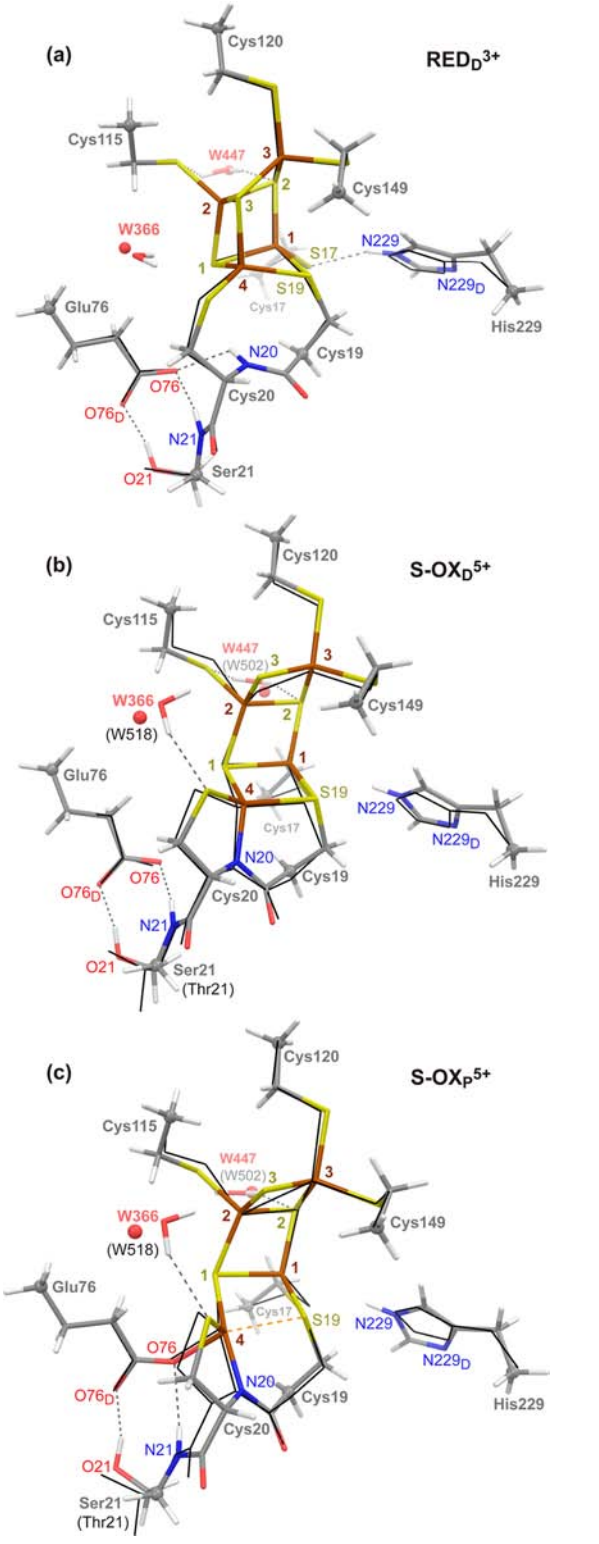

Figure 4. Representative PBE-optimized models of the MBH proximal cluster compared to reference structures from X-ray diffraction: (a) RED_D (from *Re* MBH PDB 3RGW), (b) $S\text{-}OX_D$, and (c) $S\text{-}OX_P$ (from the two *Ec* MBH conformers in PDB 3USC). The DFT structures are represented by 0.1 Å radius tubes, superimposed onto the respective X-ray structural reference data (black wires; red spheres for the two conserved water molecules). Hydrogen-bonding contacts within 2.5 Å are shown as gray dashed lines. The dashed orange line in (c) indicates an essentially lost Fe4−S19 coordination. The gray spheres mark α-carbon atoms fixed to their X-ray structure positions during optimization. Important interatomic distances are provided in Table 1.

dx.doi.org/10.1021/ja402159u | J. Am. Chem. Soc. 2013, 135, 11809−11823

Table 1. Important Internuclear Distances (Å) of the MBH Proximal Cluster Structures from X-ray Data Analyses and DFT Computations[a]

structure	Fe4−N20	Fe4−O76	Fe4−S3	Fe4−S19	O76−N20	O76−N21	$O76_D$-O21	N229−S17
RED_D *Re* [b]	3.29	4.64	2.32	2.31	3.08	2.84	2.50	3.31
RED_D *Hm* [c]	3.24	4.67	2.40	2.37	3.07	2.82	2.55	3.31
RED_D *Ec* [d]	3.26	4.71	2.42	2.36	3.11	2.80	2.50	3.30
Red2_24 [h]	3.50	–	2.32	2.30	–	–	–	–
RED_D^{3+}	3.34	4.79	2.43	2.38	3.08	2.78	2.65	3.43
RED_D^{4+}	3.21	4.70	2.43	2.40	3.05	2.79	2.66	3.50
RED_D^{5+}	3.35	4.71	2.39	2.43	2.96	2.80	2.67	3.55
$S\text{-}OX_D$ *Hm* [e]	2.09	3.06	4.01	2.51	3.09	3.08	2.43	3.33
$S\text{-}OX_{D/P}$ *Ec* [f]	2.13/2.15	4.13/2.07	3.99/4.33	2.29/2.89	3.85/2.82	3.35/3.33	2.42/2.77	3.23/3.23
$PC3_d^-$/PC3$^-$ [g]	1.95/1.99	3.79/2.05	4.15/4.67	2.43/2.74	3.39/2.86	–	–	–
Ox2_24 [h]	1.93	–	4.82	2.43	–	–	–	–
$S\text{-}OX_{D/P}^{5+}$	1.97/2.03	3.98/2.10	4.26/4.80	2.41/2.67	3.36/2.75	2.80/3.23	2.64/2.71	3.53/3.55
$PC3^H$ [g]	1.98	2.40	4.20	2.46	2.90	–	–	–
$S\text{-}OX_{D\text{-}H}^{3+}$	2.08	5.13	3.99	2.39	5.01	4.90	2.82	3.38
$S\text{-}OX_{D\text{-}H}^{4+}$	2.02	5.14	4.02	2.37	5.01	4.89	2.84	3.42
$S\text{-}OX_{D\text{-}H}^{5+}$	2.00	4.71	4.06	2.38	4.16	3.56	2.75	3.59
TS^{3+}	2.36	3.20	3.91	2.37	2.54	3.41	2.76	3.41
TS^{4+}	2.26	3.00	4.13	2.36	2.53	3.41	2.80	3.51
TS^{5+}	2.19	3.10	4.09	2.38	2.53	3.45	2.81	3.54
RED_P^{3+}	3.07	2.25	3.96	2.42	2.82	3.76	2.75	3.45
RED_P^{4+}	3.00	2.15	4.16	2.44	2.83	3.86	2.80	3.57
RED_P^{5+}	2.82	2.03	4.32	2.47	2.80	3.82	2.85	3.64

[a]Atom labels are as in Figures 2−7. Structure names with two-letter codes *Re*, *Hm*, and *Ec* correspond to X-ray data on MBHs from species *Ralstonia eutropha*, *Hydrogenovibrio marinus*, and *Escherichia coli*, respectively. Structure names with the charge 3+/4+/5+ superscript are from the present modeling using the PBE functional. '–' designates distances which were not reported. [b]PDB 3RGW[24] (1.50 Å resolution). [c]PDB 3AYX[25] (1.18 Å). [d]PDB 3UQY[26] (1.47 Å). [e]PDB 3AYY[25] (1.32 Å). [f]PDB 3USC[26] (2.00 Å); D/P subscripts correspond to A/B Glu76 and C/B Fe4 positions, each with 0.5 B-factor, as found in PDB 3USC. [g]Structures from the QM/MM modeling by Volbeda et al.[26] [h]Representative structures from the DFT modeling by Pandelia et al.[45]

somewhat inferior to the match for the RED_D^{3+} state (see **B** above), with ∼0.2 Å deviations in important internuclear distances (Table 1). This may be rationalized by (*i*) our construction of the $S\text{-}OX_D$ state (structurally characterized for the *Ec* MBH) based on the RED_D X-ray structure (from the *Re* MBH), and (*ii*) the apparent population of the two $S\text{-}OX_{D/P}$ arrangements within a single X-ray-data electron-density map.

The *Ec* MBH $S\text{-}OX_D$ arrangement[26] differs from the original *Hm* structure determination[25] mainly in the relative positions of the Glu76 carboxylate and Fe4 (see Table 1). The presently optimized Fe4−O76 distance in $S\text{-}OX_D^{5+}$ is ∼4.0 Å and falls into the range refined to ∼3.8 and ∼4.1 Å by Volbeda et al.[26] for the *Hm* and *Ec* MBH structures, respectively. The *Hm* MBH $S\text{-}OX_D$ Fe4−O76 distance before the additional refinement is ∼3.1 Å, clearly differing significantly. The very first structural determination of the superoxidized proximal cluster from *Hm* MBH may apparently be viewed as a density distribution to which both the $S\text{-}OX_D$ and $S\text{-}OX_P$ configurations contribute.

Compared to the RED_D^{3+} structure, we obtain Fe4−O76 to be ∼0.8 Å shorter in $S\text{-}OX_D^{5+}$, representing an increased electrostatic attraction between the negative Glu76 carboxylate and the superoxidized $[4Fe\text{-}3S]^{5+}$ iron−sulfur core. This corresponds well to ∼05−0.6 Å decrease of the Fe4−O76 distance from the X-ray data. Finally, our $S\text{-}OX_D^{5+}$ setup corresponds to a QM/MM model ($PC3_d^-$) studied earlier.[26] The two independent DFT optimizations provide similar structural details (Table 1).

$S\text{-}OX_P^{5+}$. The recently proposed coordination of the Glu76 carboxylate to Fe4 (Figure 3) was considered in our $S\text{-}OX_P^{5+}$ model. To optimize this state, initially an artificial harmonic attractive potential (as implemented in JAGUAR) was introduced between the Fe4 and O76 nuclei (which are separated by ∼4.0 Å in the $S\text{-}OX_D^{5+}$ model, see above). The structure was then reoptimized without the attractive potential, resulting in the desired local minimum, where Fe4−O76 bonding is apparent from a distance of ∼2.1 Å (Figure 4c). $S\text{-}OX_P^{5+}$ matches well the superoxidized *Ec* MBH X-ray data refinement results by Volbeda et al.,[26] as well as their $PC3^-$ QM/MM model (Table 1). Similarly to the S3-to-N20 Fe4 ligand substitution observed during optimization of the $S\text{-}OX_D^{5+}$ model, we notice a S19-to-O76 exchange for $S\text{-}OX_P^{5+}$: Fe4 moves ∼0.3 Å away from the thiolate of the supernumerary Cys19 toward the Glu76 carboxylate oxygen atom. This results in a Fe4−S19 distance of ∼2.7 Å, and the bonding is essentially lost. The corresponding distance from the MBH X-ray analyses is ∼2.5 Å for *Hm* species ($S\text{-}OX_D$ before the additional refinement)[25] and ∼2.9 Å for *Ec* (refined to $S\text{-}OX_P$).[26] Figure 5 provides an alternative structural comparison of our S-OX models, where Fe4−N20 coordination is present: relative to the fixed α-carbons framework, the O76 carboxylate oxygen atom displacement is ∼1.1 Å between $S\text{-}OX_D^{5+}$ and $S\text{-}OX_P^{5+}$. Simultaneously, S19 of the [4Fe-3S] core shifts toward Fe4

dx.doi.org/10.1021/ja402159u | J. Am. Chem. Soc. 2013, 135, 11809−11823

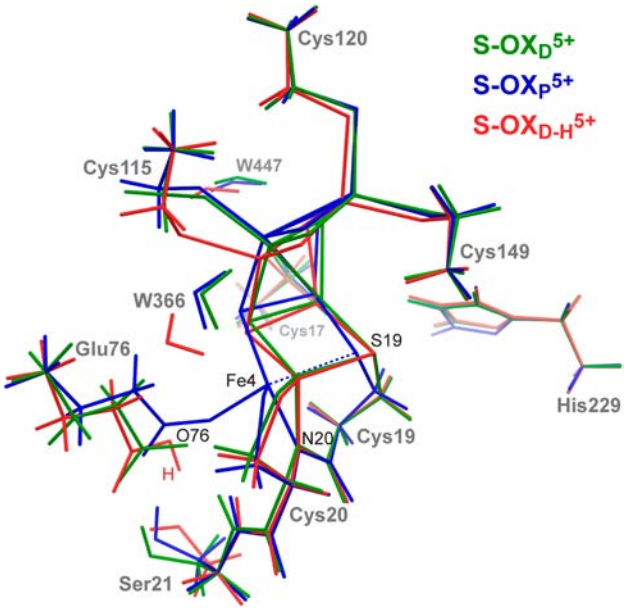

Figure 5. Overlay of the $[4Fe\text{-}3S]^{5+}$ superoxidized proximal cluster models exhibiting coordination of the Cys20 backbone amide N20 to the 'special' iron site Fe4: S-OX$_D^{5+}$ (green), S-OX$_P^{2+}$ (blue), and S-OX$_{D\text{-}H}^{5+}$ (red), shown in tubes with 0.05 Å radius. The eight α-carbons nuclei fixed to their X-ray positions during structure optimization (as shown in Figure 4) are superimposed.

by ~0.5 Å in S-OX$_P^{5+}$. Finally, the absolute ~0.9 Å Fe4 displacement between the S-OX$_D^{5+}$ and S-OX$_P^{5+}$ states is consistent with a corresponding ~0.7 Å shift obtained from the X-ray data refinement.

Notably, the S-OX$_D^{5+}$ and S-OX$_P^{5+}$ models are equivalent in their set of atoms and total charge, and we may thus compare their DFT energies. At PBE level, the S-OX$_P^{5+}$ structure is favored by 1.6 kcal/mol. This is certainly below the inherent DFT accuracy on relative energies, sometimes estimated to be 3−5 kcal/mol for the studied type of systems.[59] In contrast to the quality of computed structures (see above in **B**), the relative energies are often better represented by hybrid functionals such as B3LYP.[59,70] Reoptimization of the S-OX$_{D/P}^{5+}$ pair using B3LYP favors the S-OX$_P^{5+}$ isomer by 5.1 kcal/mol. The relatively small energy difference between S-OX$_D^{5+}$ and S-OX$_P^{5+}$ suggests an appreciable mobility of the Glu76 side chain. As the energy profile is flat, we also estimate a relatively small barrier for this interconversion, consistent with a thermal equilibrium between S-OX$_D$ and S-OX$_P$ in Figure 2.

S-OX$_{D\text{-}H}^{5+}$. Similarly to the reduced RED$_D^{3+}$ state, the Glu76 carboxylate is deprotonated in the S-OX$_{D/P}^{5+}$ models considered above. However, the Glu76 O76 oxygen atom is in close contact to the N20 amide (O76−N20 ~3.1 Å in RED$_D$) and may serve as proton acceptor from this backbone nitrogen atom during the redox process.[25,26] A model S-OX$_{D\text{-}H}^{5+}$, where O76 is protonated, is therefore another alternative for the S-OX$_D$ X-ray structure. Optimization of such a model results in a larger distance of the Glu76 carboxyl from the cluster core compared to S-OX$_D^{5+}$ (see Figure 5 and Table 1). The characteristic Fe4−O76 distance in S-OX$_{D\text{-}H}^{5+}$ is ~4.7 Å. This somewhat differs from the ~3.8−4.1 Å refined for S-OX$_D$ and ~4.0 Å optimized for our S-OX$_D^{5+}$ model. The moderate carboxylate displacement in S-OX$_{D\text{-}H}^{5+}$ is due to the diminished electrostatic attraction to the cluster core upon protonation of O76. The shifts of the Cys115 side chain and of W366 seen in Figure 5 for S-OX$_{D\text{-}H}^{5+}$ can also be rationalized from this modified charge distribution. Our S-OX$_D^{5+}$ model with the deprotonated Glu76 carboxylate is thus preferred over S-OX$_{D\text{-}H}^{5+}$ as a candidate for the S-OX$_D$ structure. The importance of the S-OX$_{D\text{-}H}^{5+}$ model will however be reexamined in **D** below.

S-OX$_{P\text{-}H}^{5+}$. In view of the Fe4−O76 coordination present in the S-OX$_P$ state, only the Glu76 carboxylate oxygen atom O76$_D$ distal to Fe4 can be considered for protonation here. A corresponding QM/MM model was discussed by Volbeda et al.[26] and named PC3^H. This would correspond to S-OX$_{P\text{-}H}^{5+}$ in our nomenclature. The PC3^H model was reported to provide an Fe4−O76 distance of ~2.4 Å, which is somewhat larger than the ~2.1 Å obtained from the X-ray structure refinement and our S-OX$_P^{5+}$ modeling (Table 1). As detailed in the Introduction, PC3^H is also problematic because of ~0.4 Å underestimation of the Fe4−S19 distance (2.46 Å optimized vs 2.89 Å in S-OX$_P$). All present efforts to locate the S-OX$_{P\text{-}H}^{5+}$ minimum were not successful. Protonation of the Glu76 at O76$_D$ makes the carboxylate a weaker metal ligand, which results in a loss of the Fe4−O76 coordination contact. This produces a state similar to the S-OX$_{D\text{-}H}^{5+}$ already described, but with O76$_D$ protonated instead of O76. Variation of the density functional (as explained in **B** for RED$_D^{3+}$) did not change this result.

D. Redox-Dependent Structural Transformation. The above models are considered in the context of the structures obtained from the X-ray data analyses of various MBH crystals under specific chemical conditions. What is the relevance of these models to the *in vivo* proximal cluster rearrangement? At which oxidation level(s) among the three $[4Fe\text{-}3S]^{3+/4+/5+}$ alternatives may this transformation take place, and what are the associated energetics? Here we propose a mechanistic scenario for this process.

RED$_D^{5+}$. The $[4Fe\text{-}3S]^{3+/4+}$ redox transition corresponds to the 'normal' function of the proximal cluster, mediating the electron transfer from the bimetallic active site during the H_2 oxidation by [NiFe]-hydrogenases. As will be shown below, under physiological conditions superoxidation to $[4Fe\text{-}3S]^{5+}$ is necessary to trigger the major RED → S-OX structural transformation, relevant for the cluster in MBH. As explained in the Introduction, O_2 binding to the [NiFe] active site induces a *swift* donation of two electrons from the proximal cluster in order to avoid the detrimental Ni-A species. It thus seems reasonable to assume that *immediately* prior to the switch to the S-OX structure, the proximal cluster has lost two electrons but still is in the structural arrangement with the RED conformation. In terms of our modeling (see **B** above), this implies a fast RED$_D^{3+}$ − 2e^- → RED$_D^{5+}$ oxidation, followed by a slower structural transformation. Indeed, optimization of a corresponding RED$_D^{5+}$ model has been successful. It exhibits only minor structural deviations from the reduced RED$_D^{3+}$ state, as detailed in Table 1 and shown in Figure S2 of Supporting Information.

TS^{5+}. It may thus be assumed that the structural transformation proceeds from this RED$_D^{5+}$ reactant on the potential energy surface (PES) of the superoxidized $[4Fe\text{-}3S]^{5+}$ cluster. In RED$_D^{5+}$, the Glu76 carboxylate oxygen atom O76 is ~3.0 Å from N20 of the Cys20 backbone. This is an appropriate position to accept the N20 proton. We located a transition state TS^{5+}, where the Glu76 side chain shifts to exchange the main hydrogen bonding partner of O76 from N21 (from the Ser21 backbone) to N20 and simultaneously abstracts the proton

dx.doi.org/10.1021/ja402159u | J. Am. Chem. Soc. 2013, 135, 11809−11823

from N20 (Figure 6). At the transition state, the proton is approximately on the line between O76 and N20, and the key

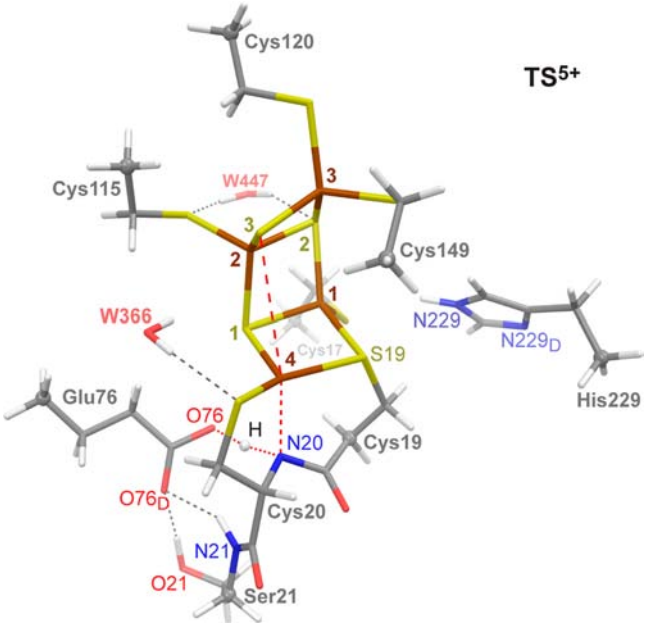

Figure 6. Optimized model for the TS^{5+} transition state of the MBH proximal cluster structural transformation. The red broken lines indicate covalent bonding rearrangements during the proton (shown as white sphere) transfer from the N20 amide to the O76 carboxylate oxygen, concerted N20 coordination to Fe4, and Fe4−S3 coordination loss (N20−H = 1.37 Å, O76−H = 1.19 Å, Fe4−N20 = 2.19 Å, Fe4−S3 = 4.09 Å). The rest of the figure details are as in Figure 4.

distances are N20−H ∼1.4 Å, O76−H ∼1.2 Å, and O76−N20 ∼2.5 Å. In concert with this proton transfer, (*i*) the Fe4−N20 bonding develops (distance ∼2.2 Å), accompanied by a pyramidalization of the Cys20 amide, and (*ii*) *trans* to N20, the inorganic S3 sulfur ligand of Fe4 is lost, leading to an extra opening of the [4Fe-3S] core with Fe4−S3 ∼4.1 Å. A visualization of the normal mode corresponding to the relevant TS^{5+} i883 cm^{-1} imaginary frequency is provided as Supporting Information. Using the PBE functional, the energy of TS^{5+} is +17.1 kcal/mol relative to the RED_D^{5+} reactant (≡0.0 kcal/mol). The product of this rearrangement is the $S\text{-}OX_{D\text{-}H}^{5+}$ state addressed in **C** above. It is at +1.4 kcal/mol relative to the RED_D^{5+} reactant (PBE data).

RED_P^{5+}. At TS^{5+}, O76 is at ∼3.1 Å from Fe4, closer than either at the RED_D^{5+} reactant or the $S\text{-}OX_{D\text{-}H}^{5+}$ product (Table 1). Yet, no O76−Fe4 bonding is present, in contrast to the $S\text{-}OX_P$ structure (see above). We have located another minimum on the $[4Fe\text{-}3S]^{5+}$ PES, which is structurally close to RED_D^{5+} but has developed Glu76−Fe4 bonding with the shortest Fe4−O76 distance of ∼2.0 Å among the models we optimized (Figure 7). It has lost the Fe4−S3 contact but still exhibits protonated N20. A somewhat weakened Fe4−S19 contact at ∼2.5 Å can still be interpreted as a preserved bond. This RED_P^{5+} structure has no correspondence to any of the so far known X-ray structure determinations, but is only +5.2 kcal/mol above RED_D^{5+} (using PBE). With its acceptable relative energy and apparent ∼2.8 Å O76−N20 hydrogen bonding, RED_P^{5+} can be considered potentially as an intermediate preceding the proton transfer from N20 during the course of the cluster transformation. However, a transition state that

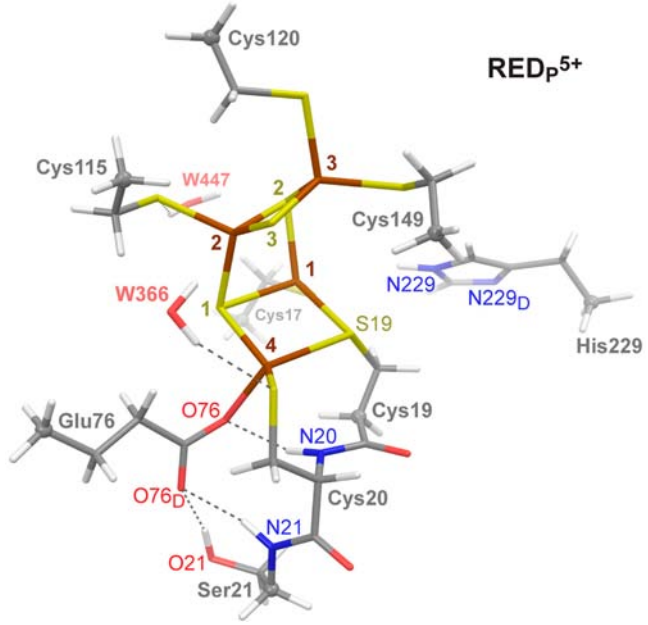

Figure 7. Optimized model for the RED_P^{5+} local minimum of the superoxidized proximal cluster. The figure details are as in Figure 4.

would directly lead from RED_P^{5+} to the $S\text{-}OX_{D\text{-}H}^{5+}$ product has not been found during our exploration of the PES. Starting from RED_P^{5+}, the second Glu76 carboxylate oxygen atom $O76_D$ distal to Fe4 may be considered as an alternative proton acceptor from N20. However, we do not anticipate this option as feasible in view of an extended, ∼3.9 Å $O76_D$-N20 internuclear separation, and a restricted ability of the Fe4-bound carboxylate to further approach the N20 amide. We will nevertheless come back to the RED_P structure further below.

E. Energetics of the Structural Transformation at the Three $[4Fe\text{-}3S]^{3+/4+/5+}$ Oxidation Levels. PBE vs B3LYP Results. From our PBE results, the $RED_D^{5+} \rightarrow TS^{5+} \rightarrow S\text{-}OX_{D\text{-}H}^{5+}$ transformation characterized above for the $[4Fe\text{-}3S]^{5+}$ superoxidized proximal cluster is an almost thermoneutral process. The calculated 17.1 kcal/mol TS^{5+} activation barrier (PBE) is relatively high for enzyme kinetics, but still in an acceptable range. We have been able to locate the associated minima and (approximate) transition states for this process not only on the superoxidized $[4Fe\text{-}3S]^{5+}$ PES, but also on the one-electron oxidized $[4Fe\text{-}3S]^{4+}$ and reduced $[4Fe\text{-}3S]^{3+}$ PESs (see Figure S2 and Table 1 for the structural details). The relative energies of the optimized $S\text{-}OX_{D\text{-}H}^{4+}$ (+13.6 kcal/mol vs RED_D^{4+}) and $S\text{-}OX_{D\text{-}H}^{3+}$ (+23.1 kcal/mol vs RED_D^{3+}) suggest that each one-electron reduction step destabilizes the $S\text{-}OX_{D\text{-}H}$ product structure by roughly ∼10 kcal/mol (PBE data, Figure 8a). This translates into a factor of $\sim 10^{-7}$ in relative populations at room temperature. Already for the one-electron oxidized cluster, the $S\text{-}OX_{D\text{-}H}^{4+}$ product is thus strongly disfavored. To reduce the computational effort, the approximate $TS^{4+/3+}$ transition state structures were optimized starting from the TS^{5+} model (Figure 6), adding $1e^-/2e^-$, respectively, while fixing the N20−H = 1.37 Å and O76−H = 1.19 Å distances corresponding to the proton transfer. In line with the increase of the relative energies of the $S\text{-}OX_{D\text{-}H}^{4+/3+}$ products, the $TS^{4+/3+}$ activation barriers also increase to over 20 kcal/mol and become prohibitively high for enzyme catalysis.

As hybrid functionals are expected to offer superior quality activation barriers compared to a pure GGA functional like

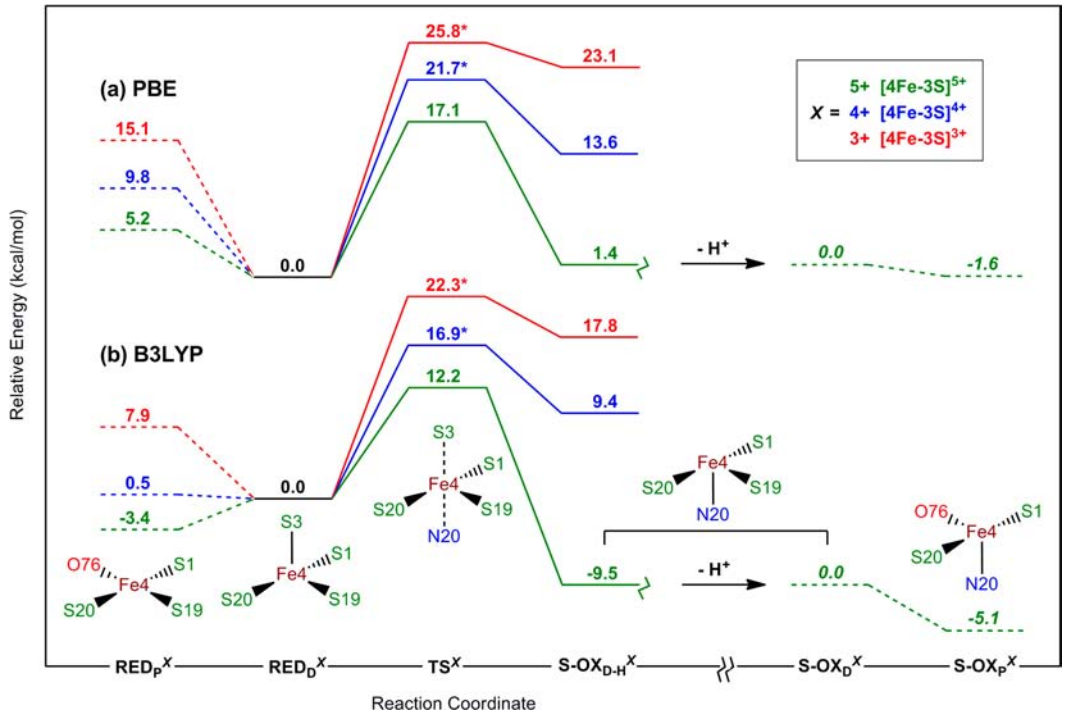

Figure 8. Relative energy profiles obtained for the MBH proximal cluster structural transformations at the superoxidized (green), oxidized (blue), and reduced (red) oxidation levels using (a) PBE and (b) B3LYP density functionals. The 'special' Fe4 iron coordination sphere is schematically shown for every state. '-H^{+}' implies deprotonation of the Glu76 O76 oxygen in the S-$OX_{D\text{-}H}^{5+}$ state and discontinuity of the potential energy surface (PES). The key transformation involving the TS transition state is given in solid line, and the rest of the relative energies are shown as dashed lines. The asterisks (*) denote approximate TS transition states as described in the text.

PBE,[59,70] we also provide the energetics at the B3LYP level (Figure 8b) after reoptimization of all relevant models. While the PBE and B3LYP energy profiles are qualitatively similar, several notable differences arise. Specifically, (*i*) relative to the $RED_D^{5+/4+/3+}$ reactant references, B3LYP gives ∼3−5 kcal/mol lower activation energies. Most importantly, the 12.2 kcal/mol TS^{5+} barrier on the superoxidized PES is now clearly appropriate for enzyme catalysis. (*ii*) The thermodynamic driving force of the reaction is enhanced on all three PESs; in particular, the S-$OX_{D\text{-}H}^{5+}$ product becomes favorable by 9.5 kcal/mol relative to RED_D^{5+}. Finally, (*iii*) RED_P^{5+} is slightly (3.4 kcal/mol) below the RED_D^{5+} reactant. A lowering of the barriers for B3LYP vs PBE is not a very common result, as very often barriers are rather increased by exact-exchange admixture to the functional. It appears that a substantial destabilization of the $RED_D^{5+/4+/3+}$ reactant occurs when using B3LYP vs PBE, as confirmed also by the lower relative energies of the S-$OX_{D\text{-}H}^{5+/4+/3+}$ product minima.

The energy profiles in Figure 8 provide a clear mechanistic scenario for the structural reorganization of the proximal cluster associated with the electron-transfer processes. In agreement with experimental observation, the reduced $[4Fe\text{-}3S]^{3+}$ proximal cluster may only be found in its single RED_D conformation.[24−26] Removal of one electron reduces the activation barrier for structural transformation, but the rearrangement remains energetically unfavorable. Only removal of two electrons renders the reorganization kinetically *and* thermochemically feasible.

The role of coordination of Glu76 to Fe4 for the overall process remains uncertain, but the corresponding structures are at least energetically accessible. We note in passing that at the B3LYP level, the energy of RED_P^{4+} differs only by 0.5 kcal/mol from that of RED_D^{4+}. It is possible that such a $RED_D^{4+} \rightleftharpoons RED_P^{4+}$ interconversion involving mobility of Glu76 may apply to the least well understood $S = 0$ $[4Fe\text{-}3S]^{4+}$ intermediate cluster oxidation level.

F. Reverse Transformation of the Cluster. The B3LYP results in Figure 8b suggest that the superoxidized cluster will be 'locked' in the S-$OX_{D\text{-}H}^{5+}$ configuration, as the reverse reaction would require a too high 9.5 + 12.2 = 21.7 kcal/mol activation energy, and the back-transformation would also be thermodynamically uphill. Moreover, it may be assumed that the proton accepted by Glu76 from N20 in the forward transformation is dislocated further within a long-range proton transfer residue network (e.g., toward the active site),[25,26] a process that is outside the scope of the present modeling approach. The superoxidized proximal cluster models S-$OX_{D/P}^{5+}$ arising after such a proton transfer were already considered in **C** above (see also Figure 4b,c, and the right side of Figure 8).

We may, however, use Figure 8 to consider the structural back-transformation of the cluster to the RED_D minimum upon reduction. This should occur after the successive reactivation of the Ni−B species in the [NiFe] active site. Provided a proton is available at the Glu76 carboxylate O76 oxygen atom, both the PBE and B3LYP energetics indicate that already one-electron reduction of the superoxidized cluster is sufficient to trigger an exothermic reverse structural change starting from S-$OX_{D\text{-}H}^{4+}$ with an activation energy of 21.7 − 13.6 = 8.1 kcal/mol at PBE and 16.9 − 9.4 = 7.5 kcal/mol at B3LYP level, respectively. Concerted two-electron reduction would render the back-transformation process even more favorable, with a barrier of only a few kcal/mol and a thermochemical driving force of about 20 kcal/mol.

dx.doi.org/10.1021/ja402159u | J. Am. Chem. Soc. 2013, 135, 11809−11823

G. Influence of Dispersion Interactions. As noncovalent interactions are not well reproduced by standard DFT functionals, we have evaluated the influence of D3 dispersion corrections[62,63] for the PBE and B3LYP energy profiles in Figure 8. Initially, single-point D3 corrections were added to the relative energies (see Figure S3 and Table S3). As detailed in Supporting Information, the main changes from D3 pertain to the position of the Glu76 side chain relative to the [4Fe-3S] core. The structures having proximal Glu76-Fe4 contacts are stabilized relatively to the distal Glu76 configurations, with the largest magnitude of ∼5 kcal/mol for $[4Fe\text{-}3S]^{5+}$ at the B3LYP-D3 level. We have subsequently reoptimized the stationary points on the superoxidized PES using B3LYP-D3. The shifts in the energy profile compared to B3LYP turned out to be within 2 kcal/mol only (Figure 8b, $[4Fe\text{-}3S]^{5+}$ vs Table S4). Overall, the changes in relative energies from dispersion corrections are minor, and do not modify our main conclusions on the redox-dependent RED ⇌ S-OX mechanism.

H. Reorganization Energies for the 'Closed' RED_D Cluster Arrangement. A very small structural change of the RED_D^{3+} model upon oxidation to RED_D^{4+} and superoxidation to RED_D^{5+} (Figure S2) suggests small proximal cluster reorganization energies λ for the initial electron transfer. Following Marcus theory,[73] λ corresponds to the energy required to relax the structure and its environment following the electron transfer. Our computed inner-sphere contributions λ_i to the reorganization energies (see Supporting Information) for the RED_D structure are $\lambda_i^{3+\rightarrow4+}$ = 5.3 kcal/mol, $\lambda_i^{4+\rightarrow5+}$ = 4.6 kcal/mol, and $\lambda_i^{3+\rightarrow5+}$ = 13.2 kcal/mol (for the concerted two-electron process). Both $\lambda_i^{3+\rightarrow4+}$ and $\lambda_i^{4+\rightarrow5+}$ one-electron reorganization energies are close to the 4.5 kcal/mol obtained using a similar approach for the $[4Fe\text{-}4S]^{5+/4+}$ redox couple of the iron−sulfur cubane from *Pyrococcus furiosus* ferredoxin.[60]

The MBH proximal cluster in its 'closed' RED_D conformation (corresponding to the H_2-reduced structures determined crystallographically) therefore exhibits similarly small one-electron reorganization energies as the more common [4Fe-4S] clusters of comparable size, functioning as electron-transfer mediators.

Notably, the computed reorganization energies may vary significantly depending on the treatment of the environment.[74−76] The pioneering DFT study[74] on the reorganization energies in iron−sulfur clusters suggests that λ_i is approximately halved when the protein is included. Our own inner-sphere λ_i values account for the protein environment via the addition of solvent effects, fixation of backbone α-carbon atoms (carefully examined in **B**), and inclusion of the second shell ligands to the [4Fe-3S] core.

I. Dependence on Broken-Symmetry State. Our initial PBE screening of different BS states for the various local minima at the three $[4Fe\text{-}3S]^{3+/4+/5+}$ oxidation levels suggested the BS12 state to be the lowest or almost the lowest (+1.5 kcal/mol at most) in energy among the six BS alternatives available (see Computational Methods and Table S5 in Supporting Information). Moreover, the BS12 state is made plausible by the 'nested' Fe spin-coupling Scheme 1 of the superoxidized S = 1/2 cluster: the sites Fe1 and Fe2 provide the shortest Fe−Fe internuclear distance (∼2.6 Å) in the S-OX cluster conformation and form the mixed-valence $[2Fe^{2.5+}\downarrow]$ pair with the subsystem spin S_{12} = 9/2. The ferric Fe3 site in the open corner of the distorted cubane is then coupled antiferromagnetically to the $[2Fe^{2.5+}\downarrow]$ dimer, producing S_{123} = 2. Finally the 'special' ferric Fe4 site, most markedly different from typical iron centers

Scheme 1. Spin-Coupling Model for the Four Iron Sites in the Superoxidized S = 1/2 Proximal Cluster, Consistent with the Broken-Symmetry State BS12

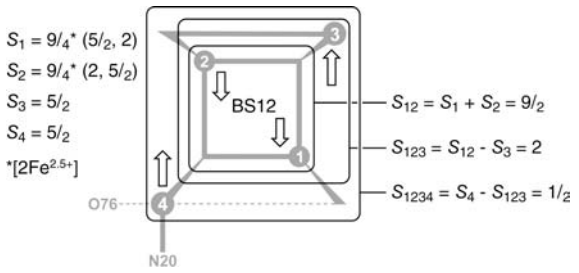

in Fe−S clusters due to the coordination by N20 (and alternatively by S19/O76 respectively in $S\text{-}OX_{D/P}$), is coupled antiferromagnetically to the [1Fe↑:2Fe↓] trimer, producing S = S_{1234} = 1/2. The relative magnitudes of the computed Fe spin populations agree well with this spin-coupling model (see Table S6, $S\text{-}OX_{D\text{-}H}^{5+}$, BS12), providing further support for our choice of the BS12 state. Therefore, BS12 was used in all calculations described above.

While two recent attempts to reconcile BS-DFT results with ^{57}Fe−Mössbauer data for the superoxidized proximal cluster from *Ae* MBH[39,45] also provided generally low relative energies for BS12 (as detailed in the Supporting Information), they favored broken-symmetry states BS13[26,44] and BS34,[45] respectively (in the present BS notation). In the most recent study favoring BS13,[44] a fully localized $Fe^{3+/2+}$ solution was proposed with no mixed-valence pair. This is rather unusual for biological iron−sulfur clusters and was based on an analysis of empty orbitals. Our computed Mulliken spin populations for the Fe sites (Table S6, $S\text{-}OX_{D\text{-}H}^{5+}$, BS13) indicate that the BS13 solution becomes valence-localized (with the $Fe^{3+/2+}$ sites at Fe3/Fe1, respectively) only when PBE is used, and appreciable delocalization is present at the B3LYP level. Another BS-DFT study[45] favoring BS34 for the $[4Fe\text{-}3S]^{5+}$ core suggests the distribution of the Fe^{3+} ferric and $Fe^{2.5+}$ mixed-valence sites equivalent to our BS12 result, but with exactly opposite Fe site spin directions relative to the total S = 1/2 spin. The authors acknowledged, however, that this interpretation of their favored model Ox2_24 (related to our model $S\text{-}OX_P^{5+}$, BS34) has the unsolved problem that the ferric sites Fe3 and Fe4 do not determine the majority spin. During revision of the present paper, a debate between the two groups appeared on the correct BS state for the superoxidized proximal cluster. Mouesca et al.[46] criticized the Ox2_24 model as an artificially trapped state with local S = 3/2 spin for ferric Fe4, instead of the expected S = 5/2. As counter-argument, Pandelia et al.[47] suggested spin-canting to explain the lower spin population at Fe4 in Ox2_24. Our own analysis (see also below) indicates that the mixed-valence solution is present for BS34 only in the 'closed' conformation, and 'opening' of the cluster leads to localization of the ferrous Fe^{2+} site at Fe4 (Table S6, BS34, RED_D^{5+} vs $S\text{-}OX_{D\text{-}H}^{5+}$). Notably, BS34 was also specified to fit best the ^{57}Fe−Mössbauer spectra for the $[4Fe\text{-}3S]^{3+}$ reduced cluster,[45] but this conclusion was based on an optimized model Red2_24 that agrees only poorly with the X-ray structure (as detailed in Supporting Information section 6). No information from experiment is available that would support any particular BS state for the $[4Fe\text{-}3S]^{4+}$ oxidized cluster.

To examine how the mechanism laid out in Figure 8 is affected by a different choice of a BS state, we have also

optimized the minima and transition states for BS13 and BS34 at the superoxidized level. A more detailed discussion and comparison of computed energy profiles is provided in Supporting Information. Here, we only note that (*i*) the BS13 state provides an almost identical energy profile to that shown in Figures 8b and S4 for the BS12 state, and (*ii*) the BS34 state gives notably higher energies (by ∼5−8 kcal/mol) for those stationary points where the Fe4−S3 bonding is lost and the cluster becomes 'opened'. The reason is the above-mentioned destabilizing Fe^{2+} valence localization at Fe4 in BS34, compared to the mixed-valence states BS12 and BS13. Only for the 'closed' RED_D^{5+} structure, all three BS12/BS13/BS34 states are nearly degenerate (within a 2.5 kcal/mol energy window, see Figure S4) and exhibit similar delocalization for the minority spin. This renders the BS34 state a less likely description of the superoxidized state, in spite of the indications from computed ^{57}Fe−Mössbauer parameters.[45]

J. Hyperfine Coupling of the Fe4-Bound Cys20 Amide Nitrogen Atom. Recent Q-band ENDOR and X-band HYSCORE studies[27,48] of the superoxidized *Re* and *Ec* MBHs reveal large nitrogen hyperfine couplings (HFC) of $A_{iso}(^{14}N)$ = 14.6 and 13.0 MHz, respectively (Table 2). These signals were labeled N_{C20} and N1, respectively, and were attributed to the Fe4-bound N20 amide. We may use these hyperfine couplings as a reference to judge the different model structures discussed above in **C** for the $[4Fe\text{-}3S]^{5+}$ superoxidized proximal cluster. In Table 2, the spin-projected hyperfine tensors obtained from the BS-DFT calculations using the BS12 broken-symmetry state (see Computational Methods and Supporting Information) are given for our three models $S\text{-}OX_P^{5+}$, $S\text{-}OX_D^{5+}$, and $S\text{-}OX_{D\text{-}H}^{5+}$, all having a Fe4−N20 bond (cf. Figure 5). The computed isotropic HFC $A_{iso}^{DFT}(^{14}N20)$ for the three models falls between 12.3 and 13.5 MHz at the PBE level, in good agreement with the experimental values. The B3LYP-based $A_{iso}^{DFT}(^{14}N20)$ is somewhat larger, 16.2−17.9 MHz for the three models. Variations between the computed $A_{iso}^{DFT}(^{14}N20)$ for the three structures are too small to be characteristic for one of them. The anisotropic part T of the HFC tensor from ENDOR is clearly rhombic,[48] in contrast to the axial T tensor from the HYSCORE study.[27] All three models reproduce the rhombic character of the anisotropic part, with $S\text{-}OX_D^{5+}$ being slightly less favorable than the two other structures. The best match between experiment and theory for the anisotropic contribution was found for the $T(^{14}N)$ tensor obtained for the *Re* MBH using ENDOR, and $T^{DFT}(^{14}N20)$ from the $S\text{-}OX_P^{5+}$ model (PBE and B3LYP results). The fact that the $S\text{-}OX_P^{5+}$-based HFC tensor agrees best with the experiment would be consistent with our proposal (above in **F**) that the $S\text{-}OX_{D\text{-}H}^{5+}$ state, when formed, swiftly loses its Glu76 carboxylate proton. When Glu76 becomes deprotonated, $S\text{-}OX_P^{5+}$ is slightly preferred over $S\text{-}OX_D^{2+}$ based on the relative energies (see **C** and Figure 8).

Complementary to the analysis of the broken-symmetry states in section I, we also examined the ^{14}N20 HFC parameters for the previously favored states BS13 and BS34. Using variations of the spin-coupling Scheme 1 (Table S7) and the B3LYP functional, for BS13 we obtained $A_{iso}^{DFT}(^{14}N20)$ values (Table S10) only slightly above those compiled in Table 2 for BS12. In contrast, the BS34 electronic structure provides a significantly weaker $A_{iso}^{DFT}(^{14}N20)$ HFC within 3.2 MHz only. This can already be deduced from the 'raw' $A_{iso}^{UBS}(^{14}N20)$ values, 34−41 MHz for BS12/BS13 vs 3−10 MHz for BS34 (Table S9).

Table 2. ^{14}N Hyperfine Parameters (MHz) of the Fe4-Bound Cys20 Amide Nitrogen Atom N20 in Different Structural Arrangements of the Superoxidized Proximal Cluster Computed using PBE and B3LYP Functionals for the BS12 Broken-Symmetry State, and Compared to ENDOR and HYSCORE Data[a]

signal/DFT model (method)	A_{iso}	T	$A = A_{iso} + T$
N_{C20} (ENDOR)[48]	14.6	[−3.2, −0.5, 3.6]	[11.4, 14.1, 18.2]
N1 (HYSCORE)[27]	13.0	[−1.5, −1.5, 3.0]	[11.5, 11.5, 16.0]
$S\text{-}OX_P^{5+}$ (PBE)	13.5	[−3.5, 0.4, 3.1]	[10.1, 13.9, 16.7]
$S\text{-}OX_P^{5+}$ (B3LYP)	17.9	[−3.8, −0.7, 4.5]	[14.1, 17.1, 22.3]
$S\text{-}OX_D^{5+}$ (PBE)	12.5	[−4.5, 1.7, 2.9]	[7.9, 14.2, 15.3]
$S\text{-}OX_D^{5+}$ (B3LYP)	16.2	[−4.9, 1.5, 3.4]	[11.3, 17.6, 19.6]
$S\text{-}OX_{D\text{-}H}^{5+}$ (PBE)	12.3	[−3.9, 0.5, 3.3]	[8.5, 12.9, 15.7]
$S\text{-}OX_{D\text{-}H}^{5+}$ (B3LYP)	16.8	[−4.6, 0.4, 4.2]	[12.3, 17.2, 21.1]

[a]HFC calculations applying the spin-projection coefficient P_{N20} = 0.47 were done as described in the Computational Methods and Supporting Information, based on the 'raw' DFT values in Table S9. A version of this table including the B3LYP results for BS13 and BS34 is available as Table S10. The structures of the $S\text{-}OX_P^{5+}$, $S\text{-}OX_D^{5+}$, and $S\text{-}OX_{D\text{-}H}^{5+}$ models are shown in Figures 4b,c and 5.

In addition to the large N_{C20}/N1 HFC, a weaker $A_{iso}(^{14}N)$ = 3.6 MHz coupling called N2 was found in the HYSCORE experiment.[27] It has been assigned to the backbone nitrogen atom of Cys19. Theoretical consideration of the N2 signal requires an extension of our present DFT model, which is under way.

IV. DISCUSSION

Our initial analysis of the different available MBH X-ray structures[24−26] indicates that the precise topology of the polypeptide framework around the [4Fe-3S] proximal cluster is highly invariant to the MBH species (see Results, **B**, and Table S1 of Supporting Information). The transformation from the 'closed' reduced (RED) to the 'opened' superoxidized (S-OX) structure (Figure 3) elicits moderate relative displacements of the α-carbon positions, commonly within 0.2 Å. The largest redox-driven relative displacements of ∼0.3 Å were found for the α-carbon atom of Cys20, which in the S-OX structure becomes coordinated to the 'special' Fe4 iron site via its N20 backbone amide nitrogen atom. The plasticity of the [4Fe-3S] iron−sulfur core is thus mostly local, and the unusual coordination by six cysteines plays a crucial role. Our present strategy of relatively large QM models ('cluster approach'), combined with a fixing of α-carbon atoms of protein residues, is well-known in many cases to provide a realistic description of metalloenzyme reaction mechanisms, alternatively to a QM/MM approach.[77,78] This appears to be well supported by the above results.

The most striking result of our computational investigation of the redox-dependent cluster rearrangement is the observation that the RED and S-OX conformations are maintained as local minima on the PES of all three $[4Fe\text{-}3S]^{3+/4+/5+}$ relevant oxidation levels of the cluster (see Results, **E**, and Figure 8). Here, we chose to couple results from the nonhybrid PBE (0% exact, or Hartee-Fock, exchange, Figure 8a) and hybrid B3LYP (20% exact exchange, Figure 8b) standard functionals. Our

dx.doi.org/10.1021/ja402159u | J. Am. Chem. Soc. 2013, 135, 11809−11823

calculations thus bracket an alternative that relies on customized functionals with 5% exact exchange, reported to optimally describe the covalence in iron−sulfur clusters.[26,72]

The computed relative energies suggest that the RED → S-OX structural transformation comes into play only upon two-electron oxidation of the proximal cluster, engaged as 'safety valve' after binding of O_2 to the [NiFe] active site. To ensure formation of the 'ready' Ni−B species (see Introduction), the active site of MBH needs to receive in total three electrons from the [4Fe-3S] proximal and [3Fe-4S] medial clusters, in a fast process. Comparison of the reduction potentials of these clusters indicates the following sequence of redox transitions:[13,15,27,28] (*i*) $[4Fe\text{-}3S]^{3+/4+}$ ($RED_D^{3+/4+}$), (*ii*) $[3Fe\text{-}4S]^{0/+1}$, and (*iii*) $[4Fe\text{-}3S]^{4+/5+}$ ($RED_D^{4+/5+}$). Both $RED_D^{3+/4+}$ and 'high-potential' $RED_D^{4+/5+}$ transitions are 'vertical' processes with small reorganization energies (see Results, **H**). Delivery of the electrons to the active site is followed by the slower RED_D^{5+} → $S\text{-}OX_{D\text{-}H}^{5+}$ structural transformation with an activation barrier of about 12−17 kcal/mol (B3LYP and PBE data in Figure 8; see Figure 6 for the TS^{5+} transition-state structure). Interestingly, the S-OX → RED back-transformation (Results, **F**) is triggered already by one-electron reduction of the superoxidized state, as indicated by a low ∼8 kcal/mol activation barrier and the appreciable exothermicity of the $S\text{-}OX_{D\text{-}H}^{4+}$ → RED_D^{4+} process. An even lower ∼3−5 kcal/mol barrier and larger thermochemical driving force for the $S\text{-}OX_{D\text{-}H}^{3+}$ → RED_D^{3+} back-transformation is apparent on the PES for the fully reduced $[4Fe\text{-}3S]^{3+}$ proximal cluster. The reduction of the superoxidized cluster either by one or two electrons therefore leads us back from the 'open' S-OX to the 'closed' RED conformation, responsible for the regular one-electron transfer function of the proximal cluster.

In line with an earlier DFT study,[45] our modeling indicates that the Glu76 carboxylate is deprotonated in the reference X-ray structures of the reduced and superoxidized proximal cluster (see Figures 4 and 5). The previously suggested[25,26] role of Glu76 as acceptor of a proton from the Cys20 backbone amide is apparent in the TS^{5+} transition state structure (Figure 6). In the initial product $S\text{-}OX_{D\text{-}H}^{5+}$ (Figures 5 and S2) of the superoxidized cluster transformation, the Glu76 carboxylate is therefore protonated. This may provide a starting point for the putative long-range proton transfer to either the [NiFe] active site or the protein surface, with Glu76 as the first link in the chain of residues involved.[25,26,42] On the other hand, both refinement of experimental electron-density maps and previous QM/MM studies[26] are consistent with the possibility of an intermediate coordination of Glu76 to Fe4 in the superoxidized state ($S\text{-}OX_{D/P}$ alternatives in Figure 3). Our results indicate that the proton at Glu76 carboxylate needs to be shuttled away to enable the Glu76-Fe4 coordination observed in the $S\text{-}OX_P$ structure. Our efforts to stabilize the Glu76-Fe4 coordination when the Glu76 is protonated (the tentative $S\text{-}OX_{P-H}^{5+}$ model), inspired by the $PC3^H$ model of Volbeda et al.,[26] were not successful. Our computations explain the structural $S\text{-}OX_{D/P}$ ambiguity of the superoxidized cluster as a thermal equilibrium between two local minima, where the coordination of the deprotonated Glu76 carboxylate to Fe4 is absent ($S\text{-}OX_D^{5+}$, Figure 4b) or present ($S\text{-}OX_P^{5+}$, Figure 4c). This equilibrium accounts for a ∼0.9 Å structural movement of Fe4 relative to the protein matrix, consistent with a displacement value of ∼0.7 Å extracted from the refined X-ray data maps. Computed relative energies indicate a small 1.6−5.1 kcal/mol preference for $S\text{-}OX_P^{5+}$ over $S\text{-}OX_D^{5+}$, almost within the error margins of BS-DFT for such energy calculations (Results, **C**). Dispersion interactions stabilize structures where the Glu76 carboxylate is proximal to the [4Fe-3S] core (by ∼4 kcal/mol at most relatively to the structures where Glu76 is distal, see Results, **G**, Figure S3, and Table S3), but do not change our conclusions for the RED ⇌ S-OX mechanistic scenario. A possible caveat regarding the relevance of the D3 correction here is that the dispersion interaction of the Glu76 side chain with the rest of the protein remains unaccounted for at our modeling level.

The flexibility of the coordination shell of the 'special' iron site Fe4 appears to be the key to the various available cluster conformations (cf. schematic representations in Figure 8). Within tetrahedral coordination, this iron site swaps its bonding between the S3 inorganic and S19 Cys19 sulfur atoms, N20 nitrogen atom of the Cys20 backbone, and also O76 oxygen atom from the Glu76 carboxylate; at the same time, the inorganic S1 and the S20 Cys20 sulfur atoms are kept by Fe4 as 'invariant' ligands.

Unexpectedly, we found that a deprotonated Glu76 carboxylate may participate in the S3-to-O76 Fe4 ligand exchange prior to deprotonation of the backbone N20 nitrogen and its coordination to Fe4. This provides yet another structure we have labeled RED_P (see Results, **D**, and Figure 7). For the reduced $[4Fe\text{-}3S]^{3+}$ cluster, the RED_P^{3+} local minimum is 8−15 kcal/mol above the RED_D^{3+} minimum and thus probably does not play a major role. At the higher $[4Fe\text{-}3S]^{4+/5+}$ oxidation levels, the electrostatic attraction between the cluster core and the negatively charged Glu76 carboxylate is enhanced, and the $RED_{D/P}^{4+/5+}$ states attain more similar energies, particularly at the B3LYP level (Figure 8b). Such an interconversion involving Glu76 side chain mobility, which had already been discussed above for the $S\text{-}OX_{D/P}^{5+}$ pair, may be specifically relevant for the less well characterized, EPR silent ($S = 0$) $[4Fe\text{-}3S]^{4+}$ oxidation state. For the superoxidized $[4Fe\text{-}3S]^{5+}$ cluster, these $RED_{D/P}^{5+}$ structures apparently decay rapidly into the $S\text{-}OX_{D\text{-}H}^{5+}$ product. Further analysis will be needed to establish a possible role of the proposed RED_P structure. Interestingly, EPR and HYSCORE data have indicated a link between the $S\text{-}OX_{D/P}$ conformations and two paramagnetic species HP1/2, which differ significantly in their electronic coupling to the [NiFe] active site.[27] By analogy, the $RED_{D/P}$ isomerism might also regulate the electron-transfer pathways involving the proximal cluster.

Shortly before the submission of this work, a QM/MM study by Mouesca et al.[44] appeared, which proposed yet another stable structure for the (super)oxidized proximal cluster. Local minima labeled $PC2[N{-}H,E76^-]/PC3[N{-}H,E76^-]$ at the $[4Fe\text{-}3S]^{4+/5+}$ oxidation levels, respectively, could be located only when more than 10% exact exchange was used for the DFT functional. These minima exhibit structures similar to our $S\text{-}OX_D^{4+/5+}$ models, but with the N20 backbone nitrogen still protonated. The Cys20 amide is thus pyramidalized in these two models, and the reported optimized Fe4−N20 distance is 2.3−2.4 Å, which is 0.2−0.3 Å larger than observed in the S-OX X-ray structures (Table 1). Starting from these $PC2[N{-}H,E76^-]$ and $PC3[N{-}H,E76^-]$ minima, PES scans for the proton transfer between the Fe4-bound N20 and Glu76 carboxylate at B3LYP level gave approximate activation barriers of 5.1 kcal/mol for the oxidized $[4Fe\text{-}3S]^{4+}$ state, and of 9.3 kcal/mol for the superoxidized $[4Fe\text{-}3S]^{5+}$ state. The products of the proton transfer, termed $PC2[N^-,E76^{O\varepsilon 1H}]/PC3\text{-}[N^-,E76^{O\varepsilon 1H}]$, are closely related to our models $S\text{-}OX_{D\text{-}H}^{4+/5+}$.

Their relative energies of 4.5/−12.0 kcal/mol, respectively, are somewhat reminiscent of our results for the S-$OX_{D\text{-}H}^{4+/5+}$ relative energies, 9.4/−9.5 kcal/mol, respectively (B3LYP results in Figure 8b). Based on the approximate activation barriers, it was concluded that the major proximal cluster transformation is more favorable to occur at the $[4Fe\text{-}3S]^{4+}$ oxidation level. However, the relatively high energy of the PC2[N^-,$E76^{O\varepsilon 1H}$] product suggests that it would immediately (activation energy 5.1 − 4.5 = 0.6 kcal/mol) transform back to the PC2[N−H,$E76^-$] reactant. In line with our results, only formation of the PC3[N^-,$E76^{O\varepsilon 1H}$] product for the $[4Fe\text{-}3S]^{5+}$ superoxidized cluster would be essentially irreversible. Finally, a comparison of the section on our PES (Figure 8b) from $TS^{4+/5+}$ to S-$OX_{D\text{-}H}^{4+/5+}$ to the results from Mouesca et al.[44] suggests that their PC2[N−H,$E76^-$] local minimum is about 5−12 kcal/mol above RED_D^{4+} (oxidized cluster), and PC3[N−H,$E76^-$] is about 2−3 kcal/mol above RED_D^{5+} (superoxidized cluster). This indicates that the starting points of the transformations chosen in ref 44 are local minima with energies higher than that of the 'closed' RED structure, in particular for the mono-oxidized $[4Fe\text{-}3S]^{4+}$ cluster.

The large $A_{iso}(^{14}N)$ = 13.0−14.6 MHz ^{14}N hyperfine coupling, that has recently been attributed to the Fe4-bound N20 nitrogen atom of the superoxidized proximal cluster by ENDOR[48] and HYSCORE[27] spectroscopies, was used as a reference that connects our computed molecular and electronic structures further to experiment (Results, **J**). This was done using spin projection, as detailed in Computational Methods and Supporting Information. For our three relevant models of the superoxidized proximal cluster (S-OX_D^{5+}, S-OX_P^{5+}, and S-$OX_{D\text{-}H}^{5+}$, see Figure 5), spin-projected BS-DFT based on the BS12 state provides $A_{iso}^{DFT}(^{14}N20)$ ∼12−18 MHz, depending on model and functional, consistent with the measured range (see Table 2). In terms of the total hyperfine tensor, the best match was obtained for $A^{DFT}(^{14}N20)$ = [10.1, 13.9, 16.7] MHz calculated for the S-OX_P^{5+} model using the PBE functional, and the $A(^{14}N)$ = [11.4, 14.1, 18.2] MHz corresponding to the N_{C20} signal from ENDOR.[48] Yet, given the dependence on exchange-correlation functional and the relatively small differences between the HFC tensors computed for the three models shown in Figure 5, the results do not allow us to sharply discriminate between these structural alternatives.

We have focused here on one particular broken-symmetry state, BS12, based on energetic, structural, and spin-coupling arguments (Results, **I** and **J**). Other recent BS-DFT studies have favored the BS13[26,44] and BS34[45] states, respectively, based on agreement with ^{57}Fe−Mössbauer data for the superoxidized cluster. For the 'forward' RED → S-OX transformation, we find here that the BS13 state gives an essentially identical energy profile as BS12 (Figure S4). In contrast, BS34 produces a valence-localized solution for the 'open' S-OX cluster conformation and is thus made less likely by 5−8 kcal/mol higher energies for transition state and product (see also Supporting Information). Additionally, while both BS12 and BS13 provide similar results for the $^{14}N20$ HFC parameters in agreement with the experiment, the calculated $A_{iso}^{DFT}(^{14}N20)$ from BS34 is at least 5-fold smaller (Table S10). For BS34, this can be rationalized as consequence of (*i*) localization of Fe^{2+} at Fe4 and (*ii*) cancellation of spin-density contributions at the N20 nucleus due to the opposite directions of the total $S = 1/2$ and local Fe4 spin vectors. Notably, none of the BS states discussed above is an entirely correct description of the cluster electronic structure. Within the BS-DFT framework, our results for the superoxidized $[4Fe\text{-}3S]^{5+}$ cluster in its 'opened' conformation are most consistent with either the BS12 or the BS13 state.

V. CONCLUSIONS

Based on structural information available from crystallography and on detailed BS-DFT calculations, we have provided a mechanistic scenario of how the unique proximal cluster of MBH functions. The low reorganization energies of the 'closed' [4Fe-3S] cluster conformation permit (*i*) its efficient electron-transfer gating function during the regular enzyme operation, and (*ii*) rapid provision of two electrons to the [NiFe] active site to prevent its overoxidation upon O_2 binding. The major structural transformation of the proximal cluster, linked to deprotonation of the Cys20 backbone amide by the Glu76 carboxylate, becomes relevant only in case (*ii*) and leads to the 'opening' of the superoxidized cluster. The 'closed' conformation is then restored upon one- or two-electron reduction of the superoxidized species, subject to the availability of a proton from the Glu76 carboxylate. The necessary structural plasticity of the proximal cluster hinges on the supernumerary coordination by six cysteines, and the flexible coordination sphere of the 'special' iron site Fe4. Future studies are anticipated to include both electron and proton transfer pathways beyond isolated views of either the bimetallic active site or the proximal cluster, thereby providing better understanding of O_2-tolerance in MBH.

■ ASSOCIATED CONTENT

Supporting Information

Details on the C_α-C_α distances, PBE vs B3LYP structures for the reduced proximal cluster, model structures at the three oxidation levels, calculation of reorganization energies, D3 dispersion corrections, BS states and their relative energies, spin populations for the Fe sites, hyperfine coupling calculations, coordinates and absolute energies of the optimized molecular systems; visualization of the normal mode corresponding to imaginary frequency of the transition state as animated GIF file. This material is available free of charge via the Internet at http://pubs.acs.org.

■ AUTHOR INFORMATION

Corresponding Author

*E-mail: pelmentschikov@mailbox.tu-berlin.de; martin.kaupp@tu-berlin.de.

Notes

The authors declare no competing financial interest.

■ ACKNOWLEDGMENTS

We gratefully acknowledge our UniCat Cluster colleagues for helpful conversations. In particular, we would like to thank Dr. Patrick Scheerer for sharing the *Re* MBH X-ray structure prior to publication, Dr. Christian Teutloff and Julia Löwenstein for discussions on their ENDOR results, and Yvonne Rippers for discussions on the DFT models. We also thank Sven de Marothy for the XYZviewer program. The research presented was supported by the Unifying Concepts in Catalysis (UniCat) Excellence Cluster in Berlin funded by Deutsche Forschungsgemeinschaft (DFG).

■ ABBREVIATIONS

BS, broken-symmetry; DFT, density functional theory; MBH, membrane-bound hydrogenase; HYSCORE, hyperfine sublevel correlation; ENDOR, electron nuclear double resonance; *Re*, *Ralstonia eutropha*; *Hm*, *Hydrogenovibrio marinus*; *Ec*, *Escherichia coli*; *Ae*, *Aquifex aeolicus*; PCET, proton-coupled electron transfer; EPR, electron paramagnetic resonance; QM/MM, quantum mechanics/molecular mechanics; SCRF, self-consistent reaction field; PCM, polarizable continuum model; HFC, hyperfine coupling; GGA, generalized gradient approximation; PES, potential energy surface

■ REFERENCES

(1) Fontecilla-Camps, J. C.; Volbeda, A.; Cavazza, C.; Nicolet, Y. *Chem. Rev.* **2007**, *107*, 4273.
(2) Lubitz, W.; Reijerse, E.; van Gastel, M. *Chem. Rev.* **2007**, *107*, 4331.
(3) Vignais, P. M.; Billoud, B. *Chem. Rev.* **2007**, *107*, 4206.
(4) Vincent, K. A.; Parkin, A.; Armstrong, F. A. *Chem. Rev.* **2007**, *107*, 4366.
(5) Siegbahn, P. E. M.; Tye, J. W.; Hall, M. B. *Chem. Rev.* **2007**, *107*, 4414.
(6) Vincent, K. A.; Cracknell, J. A.; Lenz, O.; Zebger, I.; Friedrich, B.; Armstrong, F. A. *Proc. Natl. Acad. Sci. U.S.A.* **2005**, *102*, 16951.
(7) Vincent, K. A.; Cracknell, J. A.; Clark, J. R.; Ludwig, M.; Lenz, O.; Friedrich, B.; Armstrong, F. A. *Chem. Commun.* **2006**, *48*, 5033.
(8) Wait, A. F.; Parkin, A.; Morley, G. M.; dos Santos, L.; Armstrong, F. A. *J. Phys. Chem. C* **2010**, *114*, 12003.
(9) Friedrich, B.; Fritsch, J.; Lenz, O. *Curr. Opin. Biotechnol.* **2011**, *22*, 358.
(10) Parkin, A.; Evans, R.; Roessler, M.; Fontecilla-Camps, J.; Sargent, F.; Armstrong, F. *FEBS J.* **2012**, *279*, 442.
(11) Stripp, S. T.; Goldet, G.; Brandmayr, C.; Sanganas, O.; Vincent, K. A.; Haumann, M.; Armstrong, F. A.; Happe, T. *Proc. Natl. Acad. Sci. U.S.A.* **2009**, *106*, 17331.
(12) Stiebritz, M. T.; Reiher, M. *Chem. Sci.* **2012**, *3*, 1739.
(13) Parkin, A.; Sargent, F. *Curr. Opin. Chem. Biol.* **2012**, *16*, 26.
(14) Fritsch, J.; Lenz, O.; Friedrich, B. *Nat. Rev. Microbiol.* **2013**, *11*, 106.
(15) Shafaat, H. S.; Rudiger, O.; Ogata, H.; Lubitz, W. *Biochim. Biophys. Acta* **2013**, DOI: 10.1016/j.bbabio.2013.01.015.
(16) Burgdorf, T.; Lenz, O.; Buhrke, T.; van der Linden, E.; Jones, A. K.; Albracht, S. P. J.; Friedrich, B. *J. Mol. Microbiol. Biotechnol.* **2005**, *10*, 181.
(17) Volbeda, A.; Charon, M. H.; Piras, C.; Hatchikian, E. C.; Frey, M.; Fontecillacamps, J. C. *Nature* **1995**, *373*, 580.
(18) Volbeda, A.; Montet, Y.; Vernede, X.; Hatchikian, E. C.; Fontecilla-Camps, J. C. *Int. J. Hydrogen Energy* **2002**, *27*, 1449.
(19) Buhrke, T.; Lenz, O.; Krauss, N.; Friedrich, B. *J. Biol. Chem.* **2005**, *280*, 23791.
(20) Saggu, M.; Zebger, I.; Ludwig, M.; Lenz, O.; Friedrich, B.; Hildebrandt, P.; Lendzian, F. *J. Biol. Chem.* **2009**, *284*, 16264.
(21) Goris, T.; Wait, A. F.; Saggu, M.; Fritsch, J.; Heidary, N.; Stein, M.; Zebger, I.; Lendzian, F.; Armstrong, F. A.; Friedrich, B.; Lenz, O. *Nat. Chem. Biol.* **2011**, *7*, 310.
(22) Lukey, M. J.; Roessler, M. M.; Parkin, A.; Evans, R. M.; Davies, R. A.; Lenz, O.; Friedrich, B.; Sargent, F.; Armstrong, F. A. *J. Am. Chem. Soc.* **2011**, *133*, 16881.
(23) Fritsch, J.; Loscher, S.; Sanganas, O.; Siebert, E.; Zebger, I.; Stein, M.; Ludwig, M.; De Lacey, A. L.; Dau, H.; Friedrich, B.; Lenz, O.; Haumann, M. *Biochemistry* **2011**, *50*, 5858.
(24) Fritsch, J.; Scheerer, P.; Frielingsdorf, S.; Kroschinsky, S.; Friedrich, B.; Lenz, O.; Spahn, C. M. T. *Nature* **2011**, *479*, 249.
(25) Shomura, Y.; Yoon, K. S.; Nishihara, H.; Higuchi, Y. *Nature* **2011**, *479*, 253.
(26) Volbeda, A.; Amara, P.; Darnault, C.; Mouesca, J. M.; Parkin, A.; Roessler, M. M.; Armstrong, F. A.; Fontecilla-Camps, J. C. *Proc. Natl. Acad. Sci. U.S.A.* **2012**, *109*, 5305.
(27) Roessler, M. M.; Evans, R. M.; Davies, R. A.; Harmer, J.; Armstrong, F. A. *J. Am. Chem. Soc.* **2012**, *134*, 15581.
(28) Evans, R. M.; Parkin, A.; Roessler, M. M.; Murphy, B. J.; Adamson, H.; Lukey, M. J.; Sargent, F.; Volbeda, A.; Fontecilla-Camps, J. C.; Armstrong, F. A. *J. Am. Chem. Soc.* **2013**, *135*, 2694.
(29) Lamle, S. E.; Albracht, S. P. J.; Armstrong, F. A. *J. Am. Chem. Soc.* **2004**, *126*, 14899.
(30) Vincent, K. A.; Parkin, A.; Lenz, O.; Albracht, S. P. J.; Fontecilla-Camps, J. C.; Cammack, R.; Friedrich, B.; Armstrong, F. A. *J. Am. Chem. Soc.* **2005**, *127*, 18179.
(31) Volbeda, A.; Martin, L.; Cavazza, C.; Matho, M.; Faber, B. W.; Roseboom, W.; Albracht, S. P. J.; Garcin, E.; Rousset, M.; Fontecilla-Camps, J. C. *J. Biol. Inorg. Chem.* **2005**, *10*, 239.
(32) Ogata, H.; Hirota, S.; Nakahara, A.; Komori, H.; Shibata, N.; Kato, T.; Kano, K.; Higuchi, Y. *Structure* **2005**, *13*, 1635.
(33) Ogata, H.; Kellers, P.; Lubitz, W. *J. Mol. Biol.* **2010**, *402*, 428.
(34) Soderhjelm, P.; Ryde, U. *J. Mol. Struct. (Theochem)* **2006**, *770*, 199.
(35) Siegbahn, P. E. M. *C. R. Chim.* **2007**, *10*, 766.
(36) Pavlov, M.; Blomberg, M. R. A.; Siegbahn, P. E. M. *Int. J. Quantum Chem.* **1999**, *73*, 197.
(37) Niu, S. Q.; Thomson, L. M.; Hall, M. B. *J. Am. Chem. Soc.* **1999**, *121*, 4000.
(38) Pandelia, M. E.; Fourmond, V.; Tron-Infossi, P.; Lojou, E.; Bertrand, P.; Leger, C.; Giudici-Orticoni, M. T.; Lubitz, W. *J. Am. Chem. Soc.* **2010**, *132*, 6991.
(39) Pandelia, M. E.; Nitschke, W.; Infossi, P.; Giudici-Orticoni, M. T.; Bill, E.; Lubitz, W. *Proc. Natl. Acad. Sci. U.S.A.* **2011**, *108*, 6097.
(40) Schneider, K.; Patil, D. S.; Cammack, R. *Biochim. Biophys. Acta* **1983**, *748*, 353.
(41) Knuttel, K.; Schneider, K.; Erkens, A.; Plass, W.; Muller, A.; Bill, E.; Trautwein, A. X. *Bull. Pol. Acad. Sci., Chem.* **1994**, *42*, 495.
(42) Grubel, K.; Holland, P. L. *Angew. Chem., Int. Ed.* **2012**, *51*, 3308.
(43) Peters, J. W.; Stowell, M. H. B.; Soltis, S. M.; Finnegan, M. G.; Johnson, M. K.; Rees, D. C. *Biochemistry* **1997**, *36*, 1181.
(44) Mouesca, J. M.; Fontecilla-Camps, J. C.; Amara, P. *Angew. Chem., Int. Ed.* **2013**, *52*, 2002.
(45) Pandelia, M. E.; Bykov, D.; Izsak, R.; Infossi, P.; Giudici-Orticoni, M. T.; Bill, E.; Neese, F.; Lubitz, W. *Proc. Natl. Acad. Sci. U.S.A.* **2013**, *110*, 483.
(46) Mouesca, J. M.; Amara, P.; Fontecilla-Camps, J. C. *Proc. Natl. Acad. Sci. U.S.A.* **2013**, DOI: 10.1073/pnas.1302304110.
(47) Pandelia, M. E.; Bykov, D.; Izsak, R.; Infossi, P.; Giudici-Orticoni, M. T.; Bill, E.; Neese, F.; Lubitz, W. *Proc. Natl. Acad. Sci. U.S.A.* **2013**, DOI: 10.1073/pnas.1306038110.
(48) Teutloff, C.; Löwenstein, J.; Fritsch, J.; Frielingsdorf, S.; Lenz, O.; Lendzian, F.; Bittl, R. The 45th Annual International Meeting of the EPR Spectroscopy Group of the Royal Society of Chemistry, University of Manchester, U.K., March 25−29, 2012.
(49) Perdew, J. P.; Burke, K.; Ernzerhof, M. *Phys. Rev. Lett.* **1996**, *77*, 3865.
(50) Perdew, J. P.; Burke, K.; Ernzerhof, M. *Phys. Rev. Lett.* **1997**, *78*, 1396.
(51) Lee, C. T.; Yang, W. T.; Parr, R. G. *Phys. Rev. B* **1988**, *37*, 785.
(52) Becke, A. D. *J. Chem. Phys.* **1993**, *98*, 5648.
(53) *Jaguar*, v 7.8; Schrödinger, LLC; New York, NY, 2011.
(54) Hay, P. J.; Wadt, W. R. *J. Chem. Phys.* **1985**, *82*, 299.
(55) Noodleman, L. *J. Chem. Phys.* **1981**, *74*, 5737.
(56) Noodleman, L.; Case, D. A. *Adv. Inorg. Chem.* **1992**, *38*, 423.
(57) Frisch, M. J.; Trucks, G. W.; Schlegel, H. B.; Scuseria, G. E.; Robb, M. A.; Cheeseman, J. R.; Scalmani, G.; Barone, V.; Mennucci, B.; Petersson, G. A.; Nakatsuji, H.; Caricato, M.; Li, X.; Hratchian, H. P.; Izmaylov, A. F.; Bloino, J.; Zheng, G.; Sonnenberg, J. L.; Hada, M.; Ehara, M.; Toyota, K.; Fukuda, R.; Hasegawa, J.; Ishida, M.; Nakajima, T.; Honda, Y.; Kitao, O.; Nakai, H.; Vreven, T.; Montgomery, J. A., Jr.; Peralta, J. E.; Ogliaro, F.; Bearpark, M.; Heyd, J. J.; Brothers, E.; Kudin,

K. N.; Staroverov, V. N.; Kobayashi, R.; Normand, J.; Raghavachari, K.; Rendell, A.; Burant, J. C.; Iyengar, S. S.; Tomasi, J.; Cossi, M.; Rega, N.; Millam, J. M.; Klene, M.; Knox, J. E.; Cross, J. B.; Bakken, V.; Adamo, C.; Jaramillo, J.; Gomperts, R.; Stratmann, R. E.; Yazyev, O.; Austin, A. J.; Cammi, R.; Pomelli, C.; Ochterski, J. W.; Martin, R. L.; Morokuma, K.; Zakrzewski, V. G.; Voth, G. A.; Salvador, P.; Dannenberg, J. J.; Dapprich, S.; Daniels, A. D.; Farkas, Ö.; Foresman, J. B.; Ortiz, J. V.; Cioslowski, J.; Fox, D. J. *Gaussian 09*, Revision A.02; Gaussian Inc., Wallingford, CT, 2009.

(58) Pelmenschikov, V.; Blomberg, M. R. A.; Siegbahn, P. E. *J. Biol. Inorg. Chem.* **2002**, *7*, 284.

(59) Siegbahn, P. E. M.; Blomberg, M. R. A. *Philos. Trans. R. Soc. London, Ser. A* **2005**, *363*, 847.

(60) Mitra, D.; Pelmenschikov, V.; Guo, Y. S.; Case, D. A.; Wang, H. X.; Dong, W. B.; Tan, M. L.; Ichiye, T.; Jenney, F. E.; Adams, M. W. W.; Yoda, Y.; Zhao, J. Y.; Cramer, S. P. *Biochemistry* **2011**, *50*, 5220.

(61) Tomasi, J.; Mennucci, B.; Cammi, R. *Chem. Rev.* **2005**, *105*, 2999.

(62) Grimme, S.; Antony, J.; Ehrlich, S.; Krieg, H. *J. Chem. Phys.* **2010**, *132*, 154104.

(63) Goerigk, L.; Grimme, S. *Phys. Chem. Chem. Phys.* **2011**, *13*, 6670.

(64) Beinert, H.; Holm, R. H.; Munck, E. *Science* **1997**, *277*, 653.

(65) Noodleman, L.; Lovell, T.; Liu, T. Q.; Himo, F.; Torres, R. A. *Curr. Opin. Chem. Biol.* **2002**, *6*, 259.

(66) Mouesca, J. M.; Noodleman, L.; Case, D. A.; Lamotte, B. *Inorg. Chem.* **1995**, *34*, 4347.

(67) Noodleman, L.; Peng, C. Y.; Case, D. A.; Mouesca, J. M. *Coord. Chem. Rev.* **1995**, *144*, 199.

(68) Pelmenschikov, V.; Case, D. A.; Noodleman, L. *Inorg. Chem.* **2008**, *47*, 6162.

(69) Schinzel, S.; Schraut, J.; Arbuznikov, A. V.; Siegbahn, P. E. M.; Kaupp, M. *Chem.—Eur. J.* **2010**, *16*, 10424.

(70) Neese, F. *Coord. Chem. Rev.* **2009**, *253*, 526.

(71) Pelmenschikov, V.; Siegbahn, P. E. M. *J. Am. Chem. Soc.* **2006**, *128*, 7466.

(72) Szilagyi, R. K.; Winslow, M. A. *J. Comput. Chem.* **2006**, *27*, 1385.

(73) Marcus, R. A.; Sutin, N. *Biochim. Biophys. Acta* **1985**, *811*, 265.

(74) Sigfridsson, E.; Olsson, M. H. M.; Ryde, U. *Inorg. Chem.* **2001**, *40*, 2509.

(75) Jensen, K. P. *J. Inorg. Biochem.* **2006**, *100*, 1436.

(76) Hu, L. H.; Farrokhnia, M.; Heimdal, J.; Shleev, S.; Rulisek, L.; Ryde, U. *J. Phys. Chem. B* **2011**, *115*, 13111.

(77) Siegbahn, P. E. M.; Himo, F. *Wires. Comput. Mol. Sci.* **2011**, *1*, 323.

(78) Liao, R. Z.; Thiel, W. *J. Phys. Chem. B* **2013**, *117*, 3954.